Thin-Walled Structures 152 (2020) 106375

Contents lists available at ScienceDirect

Thin-Walled Structures

journal homepage: www.elsevier.com/locate/tws

Full length article

Corotational elements for thin-walled laminated composite beams with large 3D rotations

Luiz Antonio Taumaturgo Mororó[a], Antônio Macário Cartaxo de Melo[b,*], Evandro Parente Junior[b], Eliseu Lucena Neto[c], Francisco Alex Correia Monteiro[c]

[a] Instituto Federal do Ceará, Campus Morada Nova, 62940-000, Morada Nova, Ceará, Brazil
[b] Laboratório de Mecânica Computacional e Visualização, Departamento de Engenharia Estrutural e Construção Civil, Universidade Federal do Ceará, 60455-760, Fortaleza, Ceará, Brazil
[c] Departamento de Estruturas e Edificações, Instituto Tecnológico de Aeronáutica, 12228-900, São José dos Campos, São Paulo, Brazil

ARTICLE INFO

Keywords:
Fiber reinforced composites
Thin-walled laminated beams
Finite elements
Large rotations
Corotational formulation

ABSTRACT

This work presents two finite elements for geometric nonlinear analysis of thin-walled laminated composite beams. The element cross-section properties are evaluated through a suitable thin-walled beam theory, yielding a 4×4 constitutive matrix where different couplings between generalized stresses and strains can be considered. In the local coordinate system, one element named CRL is linearly formulated, while the other element named CRTL incorporates moderate rotations. The element independent corotational approach is used in order to deal with large rotations in 3D space. Numerical experiments, considering different cross-sections and layups, demonstrate the accuracy and effectiveness of the proposed finite elements.

1. Introduction

The use of thin-walled beams in Aeronautical, Civil, Mechanical and Naval Engineering has been steadily increasing in the last decades. Due to their slenderness, such beams may present large rotations. Obviously, the analysis and design of these beams require the use of appropriate theoretical and computational tools.

In a laminated composite, each ply usually has orthotropic behavior. On the other hand, the laminated composite itself can be anisotropic due to the presence of plies with different orientations. This leads to couplings between cross-section generalized stresses and strains that do not occur in isotropic materials.

The natural approach to the structural analysis of laminated composite structures is the use of shell or solid finite elements, in which orthotropic materials with different orientations in each ply can be easily defined and the effects of transverse shear and warping can readily be considered. In addition, these elements provide directly the stresses in each ply, which can be used in the assessment of failure loads. However, the computational cost of this approach to real-world beam-like structures, as composite risers [1], is very high. This problem increases significantly when geometric nonlinear effects are considered.

Therefore, the development of beam elements for geometric nonlinear analysis of thin-walled laminated composite space frames is an important endeavor, due to their simple mesh generation and low computational cost. Several studies addressing this issue have been developed in recent years and both total and updated Lagrangian approaches have been used.

In [2], a finite element based on the total Lagrangian approach taking into account the transverse shear and warping effects was proposed to analyze thin-walled anisotropic beams with closed and open sections. In the same way, a three-dimensional frame element based on the von Kármán strains was proposed to analyze laminated box beams [3]. The effects of composite layup and structural couplings were assessed. This formulation was enhanced to consider the effects of the transverse shear strains [4].

A geometrically exact formulation was presented for analysis of thin-walled laminated beams, where the treatment of large rotation in space is accomplished by parametrization in terms of the spins (skew-matrix) [5]. This formulation leads to a non-symmetric tangent stiffness matrix and the finite element model, whose strains field is based on Green Lagrange tensor, is path-dependent and non-invariant. Note that a finite element is said invariant when has ability to not show strains when subjected to rigid body motion [6]. A space frame element for analysis of laminated thin-walled beams was proposed based on the parametrization of the finite rotations using a vector of total rotations, resulting in a path-independent and invariant element [7].

* Corresponding author.
E-mail addresses: luiz.mororo@ifce.edu.br (L.A.T. Mororó), macario@ufc.br (A.M.C.d. Melo), evandro@ufc.br (E. Parente Junior), eliseu@ita.br (E. Lucena Neto), facm@ita.br (F.A.C. Monteiro).

https://doi.org/10.1016/j.tws.2019.106375
Received 11 March 2019; Received in revised form 26 July 2019; Accepted 27 August 2019
Available online 28 May 2020

It is important to note that the effective performance of these elements depends on a careful assessment of constitutive relationship of laminated beams. Such a relationship is difficult to obtain due to the geometry of cross-section and layup of each segment of this section.

A commonly used approach for analysis of thin-walled laminated beams is to determine the equivalent sectional properties (e.g. EA, EI_y, EI_z, and GJ) by some approach, as Homogenization or Strength of Materials [8], and use these properties with conventional finite elements. One of the advantages of this approach lies in the fact that it allows the use of commercial analysis software without major changes. However, the effects of possible couplings between generalized stress and strains are neglected in this approach.

In addition to Homogenization and Strength of Materials approaches, there are several laminated beam theories in the literature that take into account all possible couplings between cross-sectional generalized stresses and strains of the classical 3D beam theory [9], including bending-torsion, bending-extension, and extension-torsion. Many of these theories, depending on the cross-section and layup, lead most likely to larger constitutive matrices than the typical ones based on Timoshenko's and Vlasov's theories for isotropic materials [10–17]. It is important to note that the element formulation and required boundary conditions become more complex for high-order models. In this case, the analysis will be computationally more expensive due to a larger number of degrees of freedom involved.

A well-known tool to obtain the section properties of laminated beams is the VABS [18]. VABS has been used in the analysis of several thin-walled beam theories [10] to conclude that in many practical cases a well formulated 4×4 matrix leads to very good results, especially for closed cross-sections. It comes from the fact that the transverse shear and restrained warping effects are not important for most laminated beams with closed cross-sections [10], for instance. Similar conclusions have also been drawn using shell elements [19]. Some recent works have successfully applied a 4×4 constitutive matrix to linear analysis, as well as nonlinear analysis restricted to moderate rotations, of laminated beams [20]. The corotational formulation has been successfully adopted for analysis of beams and shells subjected to large rotations, provided that the strains remain small [21]. The main advantage of this formulation is the possibility of exclusion of the geometric nonlinearity from the local element level. The nonlinear part is incorporated through a transformation matrix that connects local and global quantities, which are independent of the local finite element formulation. This method is very advantageous because traditional linear elements, and nonlinear elements with moderate rotations, can be easily adapted to analyses with large rotations.

In addition, the corotational approach allows the explicit separation of the kinematic quantities of the cross-section properties of laminated beams. Thus, the inherent complexities of composite beams, especially the coupling between generalized stresses and strains, are locally treated. As a consequence, simple and efficient laminated beam elements can be used at the local level.

This paper proposes two beam elements for geometric nonlinear analysis of laminated composite space frames under large rotations. These elements consider a fully coupled 4×4 constitutive matrix that is evaluated using a simple and accurate theory for thin-walled laminated composite beams with arbitrary layups [9].

The corotational approach is used in order to deal with large rotations in space in a consistent way. In the local coordinate system, two elements will be plugged into the corotational framework, one based on the linear theory (CRL element) and the other taking into account moderate rotations (CRTL element). The mathematical treatment of large rotations in space is performed by means of the rotation tensor in conjunction with the concept of pseudovector [22].

The paper is organized as follows. Section 2 is devoted to the formulations of laminated beam elements used at local level of the general corotational framework. In Section 3, some aspects related to the parametrization of finite 3D rotations and to the general element independent corotational approach for a two node beam element are discussed. Examples including large rotations are presented in Section 4 and used to assess the accuracy of the proposed elements. Finally, some conclusions are given in Section 5.

2. Element formulation

This section presents the formulation of the laminated composite beam elements to be used as local elements in the corotational framework. One element takes into account moderate rotations while the other is based on the small displacement hypothesis.

2.1. Mechanics of composite beams

The performance of the proposed finite elements depends on careful evaluation of the constitutive relation of the laminated composite beam. Such a relation is not easily obtained due to the cross-section geometry and the composite layup. Considering arbitrary layups and cross-sections, but neglecting the effects of transverse shear deformation and restrained warping, the constitutive relation for thin-walled laminated composite beams can be given by Ref. [10]:

$$\begin{Bmatrix} N \\ M_y \\ M_z \\ T \end{Bmatrix} = \begin{bmatrix} C_{11} & C_{12} & C_{13} & C_{14} \\ C_{12} & C_{22} & C_{23} & C_{24} \\ C_{13} & C_{23} & C_{33} & C_{34} \\ C_{14} & C_{24} & C_{34} & C_{44} \end{bmatrix} \begin{Bmatrix} \varepsilon_m \\ \kappa_y \\ \kappa_z \\ \beta \end{Bmatrix} \quad \Rightarrow \quad \boldsymbol{\sigma}_b = \mathbf{C}_b \, \boldsymbol{\varepsilon}_b \tag{1}$$

where N is the axial force, M_y and M_z are the bending moment about y and z axes, respectively, T is the torque, ε_m is the normal strain in the x direction, κ_y and κ_z are the beam curvatures about y and z axes, respectively, β is the rate of change of twist angle along x direction (Fig. 1), $\mathbf{C}_b$ is the constitutive matrix whose coefficients represent the beam section properties.

For an isotropic beam with doubly symmetric cross-section, the relationship in Equation (1) based on Euler-Bernoulli-Navier and Saint Venant theories results in a diagonal $\mathbf{C}_b$ matrix with $C_{11} = EA$, $C_{22} = EI_y$, $C_{33} = EI_z$, and $C_{44} = GJ$ related, respectively, to the axial rigidity, bending rigidities in the xz and xy planes, and torsional rigidity.

The beam theory proposed by Kollar and Pluzsik [9] was adopted in this work to describe the mechanics of composite laminated beams with arbitrary layups. For sake of clarity, as indicated in Fig. 2, the following orthogonal Cartesian coordinate systems are employed: xyz is the global coordinate system with origin at the mechanical centroid (point C); $\bar{x}\bar{y}\bar{z}$ is a coordinate system obtained by just translating the system locating the origin at an arbitrary point O; $x_i r_i s_i$ is the local coordinate system for the i-th segment of width b_i with origin at the center of its midsurface (point c_i). The x_i axes is parallel to the x coordinate, the s_i axes is along the segment and r_i is normal to the segment.

Considering a closed section, the cross-section of the beam consists of n flat segments (Fig. 2). Each segment may be made of several layers

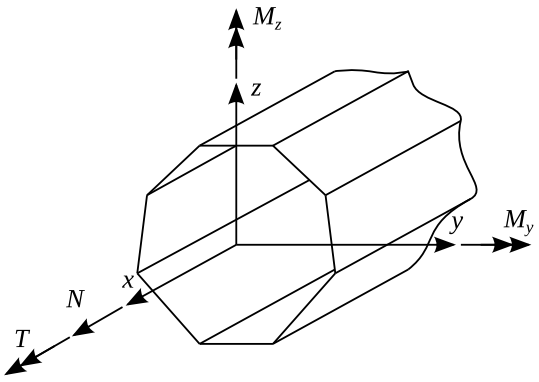

Fig. 1. Beam forces and axes.

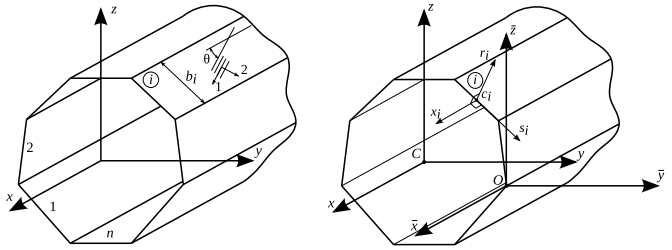

(a) (b)

Fig. 2. (a) Segments of a typical cross-section. (b) Coordinate systems.

of composite materials with arbitrary layup and is governed by the Classical Laminated Theory (CLT). Accordingly, the strain-stress relationship in the i-th segment may be written as [23,24].

$$\begin{Bmatrix} \varepsilon_x^i \\ \varepsilon_s^i \\ \gamma_{xs}^i \\ \kappa_x^i \\ \kappa_s^i \\ \kappa_{xs}^i \end{Bmatrix} = \begin{bmatrix} \alpha_{11} & \alpha_{12} & \alpha_{16} & \beta_{11} & \beta_{12} & \beta_{16} \\ \alpha_{12} & \alpha_{22} & \alpha_{26} & \beta_{21} & \beta_{22} & \beta_{26} \\ \alpha_{16} & \alpha_{26} & \alpha_{66} & \beta_{61} & \beta_{62} & \beta_{66} \\ \beta_{11} & \beta_{21} & \beta_{61} & \delta_{11} & \delta_{12} & \delta_{16} \\ \beta_{12} & \beta_{22} & \beta_{62} & \delta_{12} & \delta_{22} & \delta_{26} \\ \beta_{16} & \beta_{26} & \beta_{66} & \delta_{16} & \delta_{26} & \delta_{66} \end{bmatrix} \begin{Bmatrix} N_x^i \\ N_s^i \\ N_{xs}^i \\ M_x^i \\ M_s^i \\ M_{xs}^i \end{Bmatrix}. \tag{2}$$

When a closed section beam is cut as shown in Fig. 3, the cut edges are subjected to relative displacements that are prevented in the original beam by means of generalized forces X_1, X_2, X_3 and X_4. As proposed by Kollar and Pluzsik [9], the forces X_3 and X_4 along cut edges are generally neglected, and the shear force X_1 and bending moment X_2, which do not change along cut edges, correspond to N_{xs} and M_s in Equation (2), respectively.

Two compatibility equations must be applied to predict X_1 and X_2: the axial displacement ($u|_{left} = u|_{right}$) and the rotation ($\partial w^o/\partial s|_{left} = \partial w^o/\partial s|_{right}$) along the two cut edges must be identical. The first compatibility equation can mathematically be expressed as

$$-2A\bar{\beta} + \oint \gamma_{xs}^o \, ds = 0, \tag{3}$$

in which A is the area enclosed within the centerline of the cross-section wall, $\bar{\beta}$ is the twist rate of the longitudinal axis passing through the origin of the coordinate system $\bar{x}\bar{y}\bar{z}$, γ_{xs}^o is the shear strains of the segment on its plane. The second compatibility equation can be written by using the definition $\kappa_s = -\partial^2 w^o/\partial s^2$. Therefore,

$$\oint \kappa_s \, ds = 0. \tag{4}$$

The constitutive matrix referred to the coordinate system $\bar{x}\bar{y}\bar{z}$ reads

$$\bar{\mathbf{C}}_b = \sum_{i=1}^{n} (\mathbf{R}_i^T \, \boldsymbol{\omega}_i^{-1} \, \mathbf{R}_i) + \mathbf{L}^T \, \mathbf{F}^{-1} \, \mathbf{L} \tag{5}$$

where

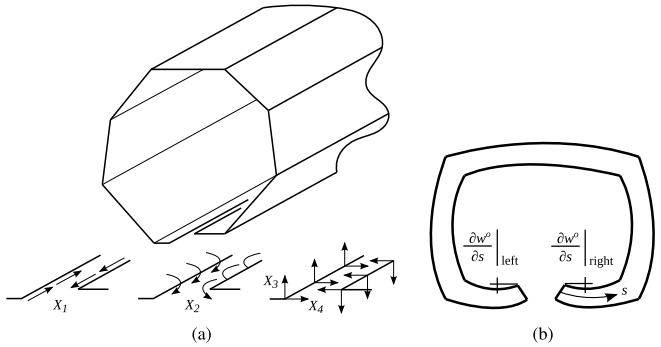

(a) (b)

Fig. 3. (a) Cut closed cross-section. (b) Rotation in cut beam: w^o is the displacement of the wall perpendicular to the segment's reference surface.

$$\boldsymbol{\omega}_i = \frac{1}{b_i} \begin{bmatrix} \alpha_{11} & \beta_{11} & 0 & -\frac{1}{2}\beta_{16} \\ \beta_{11} & \delta_{11} & 0 & -\frac{1}{2}\delta_{16} \\ 0 & 0 & \frac{12}{a_{11i}\, b_i^2} & 0 \\ -\frac{1}{2}\beta_{16} & -\frac{1}{2}\delta_{16} & 0 & \frac{1}{4}\delta_{66} \end{bmatrix} \tag{6}$$

and details on its mathematical development are given in Refs. [9,20]. The coefficient a_{11i} is computed from

$$\begin{bmatrix} a_{11} & a_{12} & a_{13} \\ a_{12} & a_{22} & a_{23} \\ a_{13} & a_{23} & a_{33} \end{bmatrix}_i = \begin{bmatrix} \alpha_{11} & \beta_{11} & \beta_{16} \\ \beta_{11} & \delta_{11} & \delta_{16} \\ \beta_{16} & \delta_{16} & \delta_{66} \end{bmatrix}_i^{-1}. \tag{7}$$

The matrices $\mathbf{F}$ and $\mathbf{L}$ are

$$\mathbf{F} = \sum_{i=1}^{n} \left(b_i \begin{bmatrix} \alpha_{66} & \beta_{62} \\ \beta_{62} & \delta_{22} \end{bmatrix}_i - \begin{bmatrix} \alpha_{16} & \beta_{61} & 0 & -\frac{1}{2}\beta_{66} \\ \beta_{12} & \delta_{12} & 0 & -\frac{1}{2}\delta_{26} \end{bmatrix}_i \boldsymbol{\omega}_i^{-1} \begin{bmatrix} \alpha_{16} & \beta_{12} \\ \beta_{61} & \delta_{12} \\ 0 & 0 \\ -\frac{1}{2}\beta_{66} & -\frac{1}{2}\delta_{26} \end{bmatrix}_i \right)$$

$$\mathbf{L} = \begin{bmatrix} 0 & 0 & 0 & -2A \\ 0 & 0 & 0 & 0 \end{bmatrix} - \mathbf{J} \tag{8}$$

where

$$\mathbf{J} = \sum_{i=1}^{n} \begin{bmatrix} \alpha_{16} & \beta_{61} & 0 & -\frac{1}{2}\beta_{66} \\ \beta_{12} & \delta_{12} & 0 & -\frac{1}{2}\delta_{26} \end{bmatrix}_i \boldsymbol{\omega}_i^{-1} \mathbf{R}_i \qquad \mathbf{R}_i = \begin{bmatrix} 1 & \bar{z}_i & -\bar{y}_i & 0 \\ 0 & \cos\alpha_i & \operatorname{sen}\alpha_i & 0 \\ 0 & -\operatorname{sen}\alpha_i & \cos\alpha_i & 0 \\ 0 & 0 & 0 & 1 \end{bmatrix}. \tag{9}$$

The matrix $\mathbf{R}_i$ relates the strain components of the i-th segment in the system $x_i r_i s_i$ to those in the system $\bar{x}\bar{y}\bar{z}$. The coordinates $\bar{z}_i$ and $\bar{y}_i$ are associated with the origin of the local system $x_i s_i r_i$ and the angle α_i is measured between the s_i and $\bar{y}$ axes (Fig. 4).

Equation (5) is focused on closed cross-sections. Nonetheless, one can obtain the constitutive matrix for open cross-sections by also neglecting the forces X_1 and X_2 in addition to X_3 and X_4. Under this assumption Equation (5) becomes

$$\bar{\mathbf{C}}_b = \sum_{i=1}^{n} (\mathbf{R}_i^T \, \boldsymbol{\omega}_i^{-1} \, \mathbf{R}_i). \tag{10}$$

Equations (5) and (10) have been developed with respect to an arbitrary coordinate system $\bar{x}\bar{y}\bar{z}$. With the coordinates of the mechanical centroid at hand, these expressions can be promptly rewritten with respect to the global coordinate system xyz. The details on this transformation as well as on how to determine such coordinates can be found in Refs. [9]. Obviously, no transformation is required for laminated cross-sections whose origin O of the arbitrary coordinate system $\bar{x}\bar{y}\bar{z}$ coincides with the mechanical centroid, where $\mathbf{C}_b = \bar{\mathbf{C}}_b$.

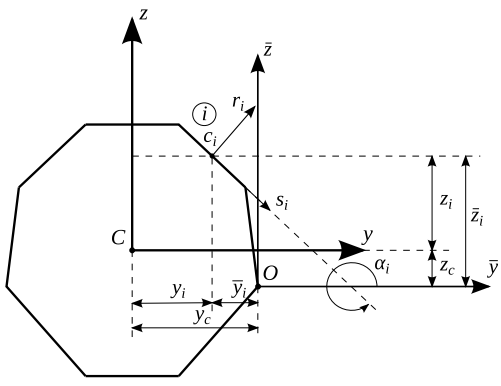

Fig. 4. Segment orientation α_i and coordinates of point c_i.

2.2. Stresses

As the beam cross-section is regarded as a collection of flat segments with arbitrary layup, the stresses at each segment are computed using the CLT. Therefore, the only concern is to transform the beam generalized stresses (N, M_y, M_z, T) into the local ones (N_x, N_s, N_{xs}, M_x, M_s, M_{xs}) per unit length.

In a closed section beam, $N_s = 0$, $N_{xs} = X_1$ and $M_s = X_2$ which can be computed from

$$\begin{Bmatrix} X_1 \\ X_2 \end{Bmatrix} = \mathbf{F}^{-1}\mathbf{L}\mathbf{C}_b^{-1}\begin{Bmatrix} \bar{N} \\ M_{\bar{y}} \\ M_{\bar{z}} \\ \bar{T} \end{Bmatrix}. \tag{11}$$

The remaining forces and moments per unit length are

$$\begin{Bmatrix} N_x \\ M_x \\ M_{xs} \end{Bmatrix}_i = \boldsymbol{\mu}_i^{-1}(\mathbf{R}_s\mathbf{R}_i - \boldsymbol{\nu}_i\mathbf{F}^{-1}\mathbf{L})\mathbf{C}_b^{-1}\begin{Bmatrix} \bar{N} \\ M_{\bar{y}} \\ M_{\bar{z}} \\ \bar{T} \end{Bmatrix} \tag{12}$$

with

$$\boldsymbol{\mu}_i = \begin{bmatrix} \alpha_{11} & \beta_{11} & \beta_{61} \\ \beta_{11} & \delta_{11} & \delta_{16} \\ \beta_{16} & \delta_{16} & \delta_{66} \end{bmatrix}_i \quad \boldsymbol{\nu}_i = \begin{bmatrix} \alpha_{16} & \beta_{12} \\ \beta_{61} & \delta_{12} \\ \beta_{66} & \delta_{26} \end{bmatrix}_i \quad \mathbf{R}_s = \begin{bmatrix} 1 & 0 & s & 0 \\ 0 & 1 & 0 & 0 \\ 0 & 0 & 0 & -2 \end{bmatrix}. \tag{13}$$

For beams with open sections, the stresses can be obtained neglecting X_1 and X_2 in the previous equations. Then, the only non-zero forces and moments per unit length are

$$\begin{Bmatrix} N_x \\ M_x \\ M_{xs} \end{Bmatrix}_i = \boldsymbol{\mu}_i^{-1}\mathbf{R}_s\mathbf{R}_i\mathbf{C}_b^{-1}\begin{Bmatrix} \bar{N} \\ M_{\bar{y}} \\ M_{\bar{z}} \\ \bar{T} \end{Bmatrix}. \tag{14}$$

2.3. Displacements and strains

The element formulation is based on Euler-Bernoulli bending and Saint Venant's torsion hypotheses. The local displacements in the x, y and z directions of a generic point P of the cross-section (Fig. 5) can then be written as

$$u = u_c - y\,v_{c,x} - z\,w_{c,x} \qquad v = v_c - z\,\theta_x \qquad w = w_c + y\,\theta_x \tag{15}$$

where u_c, v_c and w_c are the displacement components of the centroid of the cross-section, θ_x is the rotation about the x axis, the warping contribution is neglected and $\mathrm{d}(\,)/\mathrm{d}x = (\,)_{,x}$.

The CRTL element includes the effects of moderate rotations in the local system. Substitution of Equation (15) into the strain-displacement relations

$$\varepsilon_x = u_{,x} + \frac{1}{2}v_{,x}^2 + \frac{1}{2}w_{,x}^2 \qquad \gamma_{xy} = u_{,y} + v_{,x} \qquad \gamma_{xz} = u_{,z} + w_{,x}, \tag{16}$$

where the geometric nonlinearity is considered only in the axial strain

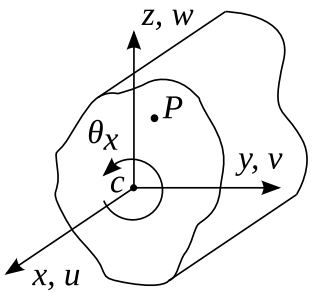

Fig. 5. Displacement of a generic point P on the cross-section.

[21], yields

$$\varepsilon_x = \varepsilon_m - y\,\kappa_z + z\,\kappa_y + y\,w_{c,x}\,\theta_{x,x} - z\,v_{c,x}\,\theta_{x,x} \qquad \gamma_{xy} = -z\,\theta_{x,x} \qquad \gamma_{xz} = y\,\theta_{x,x} \tag{17}$$

with

$$\varepsilon_m = u_{c,x} + \frac{1}{2}v_{c,x}^2 + \frac{1}{2}w_{c,x}^2 + \frac{1}{2}(y^2 + z^2)\,\theta_{x,x}^2 \qquad \kappa_y = -w_{c,xx} \qquad \kappa_z = v_{c,xx}. \tag{18}$$

Nonlinearity is only considered in the membrane strain ε_m. Thus, the last two terms ($y\,w_{c,x}\,\theta_{x,x}$ and $z\,v_{c,x}\,\theta_{x,x}$) of the axial strain in Equation (17) will be neglected. In the following, the subscript c will be dropped to simplify the notation since only displacements of the centroid appear in Equation (18).

2.4. Internal force vector

The internal virtual work is given by

$$\delta U = \int_V (\sigma_x\,\delta\varepsilon_x + \tau_{xy}\,\delta\gamma_{xy} + \tau_{xz}\delta\gamma_{xz})\,\mathrm{d}V. \tag{19}$$

Using Equation (17),

$$\delta U = \int_L \int_A (\sigma_x\,\delta\varepsilon_m - y\,\sigma_x\,\delta\kappa_z + z\,\sigma_x\,\delta\kappa_y - z\,\tau_{xy}\,\delta\theta_{x,x} + y\,\tau_{xz}\,\delta\theta_{x,x})\,\mathrm{d}A\mathrm{d}x \tag{20}$$

where the last two terms of ε_x have been neglected, and A and L are the cross-sectional area and element length, respectively.

Assuming an average normal stress $\sigma_x = N/A$ [25–27], the first term of Equation (20) becomes

$$\int_L N\,\delta\left(u_{,x} + \frac{1}{2}v_{,x}^2 + \frac{1}{2}w_{,x}^2 + \frac{1}{2}\frac{I_p}{A}\theta_{x,x}^2\right)\mathrm{d}x \tag{21}$$

where

$$I_p = \int_A (y^2 + z^2)\mathrm{d}A \tag{22}$$

is the polar moment of inertia of the cross-section. After integration in the cross section, Equation (20) yields

$$\delta U = \int_L \delta\boldsymbol{\varepsilon}_b^T\,\boldsymbol{\sigma}_b\mathrm{d}x = \int_L (N\,\delta\varepsilon_m + M_y\,\delta\kappa_y + M_z\,\delta\kappa_z + T\delta\theta_{x,x})\,\mathrm{d}x \tag{23}$$

where $\boldsymbol{\varepsilon}_b = \{\varepsilon_m\ \kappa_y\ \kappa_z\ \beta = \theta_{x,x}\}^T$ and $\boldsymbol{\sigma}_b = \{N\ M_y\ M_z\ T\}^T$.

In order to avoid membrane locking due to unbalanced terms coming from the axial and transverse displacements, ε_m in Equation (23) is replaced by its average value [21,25,26].

$$\varepsilon_m = \frac{1}{L}\int_0^L \left(u_{,x} + \frac{1}{2}v_{,x}^2 + \frac{1}{2}w_{,x}^2 + \frac{1}{2}\frac{I_p}{A}\theta_{x,x}^2\right)\mathrm{d}x. \tag{24}$$

Integrating this expression, the average membrane strain can be expressed as

$$\varepsilon_m = \frac{u_2 - u_1}{L} + \frac{1}{2L}\int_0^L v_{,x}^2\,\mathrm{d}x + \frac{1}{2L}\int_0^L w_{,x}^2\,\mathrm{d}x + \frac{I_p}{2LA}\int_0^L \theta_{x,x}^2\,\mathrm{d}x \tag{25}$$

where u_1 and u_2 are the element displacements at nodes 1 and 2, respectively.

Functions with C^0 continuity can be used to interpolate the axial displacement and the twist angle, while the transverse displacement requires the use of functions with C^1 continuity:

$$\begin{aligned} \tfrac{u_2-u_1}{L} &= [N_{1,x}\ 0\ 0\ 0\ 0\ 0\ N_{2,x}\ 0\ 0\ 0\ 0\ 0]\,\mathbf{d} = \mathbf{B}_0\,\mathbf{d} \\ v_{,x} &= [0\ H_{1,x}\ 0\ 0\ 0\ H_{2,x}\ 0\ H_{3,x}\ 0\ 0\ 0\ H_{4,x}]\,\mathbf{d} = \mathbf{B}_{bv,x}\,\mathbf{d} \\ w_{,x} &= [0\ 0\ H_{1,x}\ 0\ -H_{2,x}\ 0\ 0\ 0\ H_{3,x}\ 0\ -H_{4,x}\ 0]\,\mathbf{d} = \mathbf{B}_{bw,x}\,\mathbf{d} \\ \theta_{x,x} &= [0\ 0\ 0\ N_{1,x}\ 0\ 0\ 0\ 0\ 0\ N_{2,x}\ 0\ 0]\,\mathbf{d} = \mathbf{B}_{\theta,x}\,\mathbf{d} \end{aligned} \tag{26}$$

where $\mathbf{d}$ is the vector of nodal displacements, N_i are the linear Lagrange

polynomials and H_i are the cubic Hermite polynomials.

Using Equations (25) and (26), the average membrane strain can be written in matrix form as

$$\varepsilon_m = \left(\mathbf{B}_0 + \frac{1}{2}\mathbf{B}_L\right)\mathbf{d} = \mathbf{B}_m\mathbf{d}. \tag{27}$$

It can be noted that the bending curvatures κ_y and κ_z and twist rate $\theta_{x,x}$ are the same ones used in the traditional linear three-dimensional frame element [27]. Thus, after some mathematical manipulations, one can show that

$$\varepsilon_b = \mathbf{B}\mathbf{d} \qquad \mathbf{B} = \begin{bmatrix} \mathbf{B}_m \\ \mathbf{B}_{bw,xx} \\ \mathbf{B}_{bv,xx} \\ \mathbf{B}_{\theta,x} \end{bmatrix} = \begin{bmatrix} \mathbf{B}_0 \\ \mathbf{B}_{bw,xx} \\ \mathbf{B}_{bv,xx} \\ \mathbf{B}_{\theta,x} \end{bmatrix} + \frac{1}{2}\begin{bmatrix} \mathbf{B}_L \\ \mathbf{0} \\ \mathbf{0} \\ \mathbf{0} \end{bmatrix} \tag{28}$$

where

$$\mathbf{B}_L = \mathbf{d}^T \int_L \left(\mathbf{B}_{bv,x}^T\,\mathbf{B}_{bv,x} + \mathbf{B}_{bw,x}^T\,\mathbf{B}_{bw,x} + \mathbf{B}_{\theta,x}^T\,\mathbf{B}_{\theta,x}\right) \mathrm{d}x = \mathbf{d}^T\mathbf{A}_b. \tag{29}$$

From Equations (26) and (27)

$$\delta\varepsilon_m = (\mathbf{B}_0 + \mathbf{B}_L)\delta\mathbf{d} \qquad \delta\varepsilon_b = \bar{\mathbf{B}}\,\delta\mathbf{d} \qquad \bar{\mathbf{B}} = \begin{bmatrix} \bar{\mathbf{B}}_m \\ \mathbf{B}_{bw,xx} \\ \mathbf{B}_{bv,xx} \\ \mathbf{B}_{\theta,x} \end{bmatrix} = \begin{bmatrix} \mathbf{B}_0 \\ \mathbf{B}_{bw,xx} \\ \mathbf{B}_{bv,xx} \\ \mathbf{B}_{\theta,x} \end{bmatrix} + \begin{bmatrix} \mathbf{B}_L \\ \mathbf{0} \\ \mathbf{0} \\ \mathbf{0} \end{bmatrix}. \tag{30}$$

Finally,

$$\delta U = \delta\mathbf{d}^T\mathbf{g} \qquad \mathbf{g} = \int_L \bar{\mathbf{B}}^T\,\boldsymbol{\sigma}_b\,\mathrm{d}x \tag{31}$$

where $\mathbf{g}$ is the internal force vector.

2.5. Stiffness matrix

The use of quadratically convergent Newton-Rapshon method to solve the discrete nonlinear equilibrium equation requires the computation of the tangent stiffness matrix. The tangent stiffness matrix is obtained by differentiation of the internal force vector with respect to the nodal displacements:

$$\mathbf{k}_t = \frac{\partial\mathbf{g}}{\partial\mathbf{d}} = \int_L \bar{\mathbf{B}}^T\,\frac{\partial\boldsymbol{\sigma}_b}{\partial\mathbf{d}}\,\mathrm{d}x + \int_L \frac{\partial\bar{\mathbf{B}}^T}{\partial\mathbf{d}}\,\boldsymbol{\sigma}_b\,\mathrm{d}x = \mathbf{k}_e + \mathbf{k}_g \tag{32}$$

where $\mathbf{k}_e$ is the elastic stiffness matrix and $\mathbf{k}_g$ is the geometric (or initial stress) stiffness matrix. Recalling that $\boldsymbol{\sigma}_b = \mathbf{C}_b\varepsilon_b$, one gets from Equations (29) and (30)

$$\mathbf{k}_e = \int_L \bar{\mathbf{B}}^T\,\mathbf{C}_b\,\bar{\mathbf{B}}\,\mathrm{d}x \qquad \mathbf{k}_g = \int_L \mathbf{A}_b^T\,N\,\mathrm{d}x. \tag{33}$$

It is important to emphasize that, unlike the case of the standard beam elements, the normal force N cannot be taken out of the above integral since this force is not constant along the present element, even though the membrane strains are constant due to the use of Equation (24). The coupling terms of $\mathbf{C}_b$ matrix (C_{12}, C_{13}, C_{14}), that are generally not zero for laminated beams, explain such a variation:

$$N = C_{11}\varepsilon_m + C_{12}\kappa_y + C_{13}\kappa_z + C_{14}\beta. \tag{34}$$

According to Equation (26), the curvatures (κ_y and κ_z) depend linearly on x, while ε_m and β are constant along the element length. Therefore, the normal force can have a linear variation along the element. On the other hand, for isotropic and homogeneous beams the resulting diagonal matrix $\mathbf{C}_b$ ($C_{11} = EA$, $C_{12} = C_{13} = C_{14} = 0$) yields a constant axial force which simplifies the computation of the geometric stiffness matrix.

2.6. Small rotations

The internal force vector and stiffness matrix of the linear element CRL can be easily obtained from the nonlinear element CRTL disregarding the nonlinear terms. In this case, the strain-displacement matrix

$$\mathbf{B} = \begin{bmatrix} \mathbf{B}_0 \\ \mathbf{B}_{bw,xx} \\ \mathbf{B}_{bv,xx} \\ \mathbf{B}_{\theta,x} \end{bmatrix} \tag{35}$$

does not depend on the nodal displacements. The internal force vector Equation (31) and the stiffness matrix Equation (32) of the CRTL element reduce to

$$\mathbf{g} = \int_L \mathbf{B}^T\,\boldsymbol{\sigma}_b\,\mathrm{d}x \qquad \mathbf{k}_t = \int_L \mathbf{B}^T\,\mathbf{C}_b\,\mathbf{B}\,\mathrm{d}x. \tag{36}$$

3. Corotational formulation

The main idea of the corotational approach is to split the total displacement in a rigid body part and a deformational part. The geometric nonlinearity is considered in transformation matrices that relate the local and global quantities. The deformational part is handled by the local element. In this case, standard linear and nonlinear elements can be used in the local level. This work adopts the so-called element independent corotational approach introduced by Rankin and Brogan [28]. In this approach the transformation matrices are independent from the local element formulation [25,26,29–36], for elements with the same number of nodes and degrees of freedom.

3.1. Large rotations in space

Evaluation of 2D rotations are easier than 3D rotations, since 2D rotations are only defined by a scalar which represents the rotation magnitude about the axis perpendicular to a fixed plane. In this case, the rotations are commutative. On the other hand, large 3D rotations are much complicated because their complete treatment requires the knowledge of the rotation magnitude and the axis around which the rotation takes place. Although these two informations are commonly used to define vectors, finite 3D rotations cannot be treated as such. Switching two successive rotations about distinct axes is a simple verification of its non-vectorial aspect as can be observed that they are not commutative [37].

Mathematically, a 3D finite rotation is properly defined by an orthogonal tensor $\mathbf{R}_\theta$. There are several ways to present this tensor, leading to different parameterizations of the finite rotation tensor [37]. Felippa and Haugen [36] and Spring [38] assessed the most common parameterizations: Euler's parameters, Rodrigues' parameters, and Euler's angles.

The property $\mathbf{R}_\theta\mathbf{R}_\theta^T = \mathbf{I}$, where matrix $\mathbf{I}$ stands for the identity matrix of size 3, allows the tensor $\mathbf{R}_\theta$ to be described in terms of only three independent parameters. As proposed by Euler's theorem [36], these three parameters are the components of the pseudovector

$$\boldsymbol{\theta} = \theta\,\mathbf{e} \tag{37}$$

where θ is the rotation angle and $\mathbf{e}$ is the unit vector defining the rotation axis. The pseudovector $\boldsymbol{\theta}$ can be written in terms of its cartesian component system as

$$\boldsymbol{\theta} = \begin{Bmatrix} \theta_1 \\ \theta_2 \\ \theta_3 \end{Bmatrix} \tag{38}$$

where

$$\theta = (\theta_1^2 + \theta_2^2 + \theta_3^2)^{1/2}. \tag{39}$$

The orthogonal matrix $\mathbf{R}_\theta$ admits the following representation [22]:

$$\mathbf{R}_\theta = \mathbf{I} + \frac{\sin\theta}{\theta}\mathbf{S}_\theta + \frac{1}{2}\frac{\sin^2(\theta/2)}{(\theta/2)^2}\mathbf{S}_\theta^2 \tag{40}$$

with

$$\mathbf{S}_\theta = \begin{bmatrix} 0 & -\theta_3 & \theta_2 \\ \theta_3 & 0 & -\theta_1 \\ -\theta_2 & \theta_1 & 0 \end{bmatrix} \tag{41}$$

being the skew symmetric matrix obtained from θ. The extraction of the components of θ from $\mathbf{R}_\theta$, denoted by

$$\theta = rot(\mathbf{R}_\theta), \tag{42}$$

can be efficiently performed using the Spurrier's algorithm [39].

3.2. Kinematic description

Initially, the solid in the base configuration C_0 moves to the corotated configuration C_R through rigid body displacements (Fig. 6). After that, the deformational displacement is applied to obtain the final configuration C_D [36].

The total motion of the finite element from the base configuration C_0 to the final equilibrium configuration C_D is depicted in Fig. 7. To represent this motion, several reference systems are required:

- The global system xyz defined by the triad of unit orthogonal vectors grouped in matrix $\mathbf{I} = [\mathbf{i}\ \mathbf{j}\ \mathbf{k}]$. The equilibrium equations are referenced to this system.
- The base system $\tilde{x}\tilde{y}\tilde{z}$ defined by the triad of unit orthogonal vectors grouped in the matrix $\mathbf{T}_0 = [\mathbf{e}_{10}\ \mathbf{e}_{20}\ \mathbf{e}_{30}]$. It is defined in the configuration C_0.
- The corotational system $\bar{x}\bar{y}\bar{z}$ which continuously rotates and translates with the element. The orthogonal basis vectors are grouped in the matrix $\mathbf{T} = [\mathbf{e}_1\ \mathbf{e}_2\ \mathbf{e}_3]$ and are defined in the configuration C_R.
- The nodal systems attached to the element nodes 1 and 2. The orthogonal basis vectors are grouped in the matrices $\mathbf{A} = [\mathbf{a}_1\ \mathbf{a}_2\ \mathbf{a}_3]$ and $\mathbf{B} = [\mathbf{b}_1\ \mathbf{b}_2\ \mathbf{b}_3]$, respectively. These nodal systems rotate and translate with the respective nodal cross-sections.

The origin of the base and corotational systems are localized and fixed at node 1. The axis $\tilde{x}$ is defined by the line connecting nodes 1 and 2, whereas the axes $\tilde{y}$ and $\tilde{z}$ are attached to the principal axes of inertia of the cross-section. The corotational system orientation is defined through the rigid body motion of the base system.

It is important to introduce the adopted notation used in this work in order to better elucidate the formulation. The use of 0, R and D as superscript and subscript will indicate references to base, corotational and final configurations, respectively. Quantities with tilde and bar will

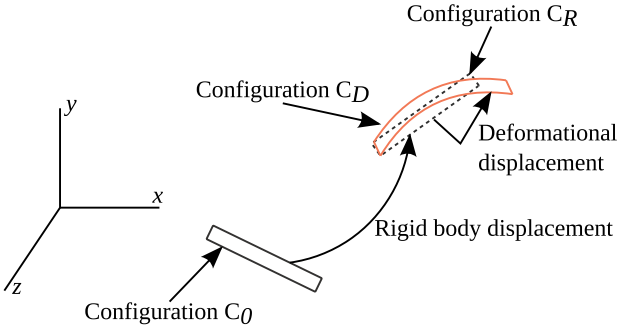

Fig. 6. Corotational description.

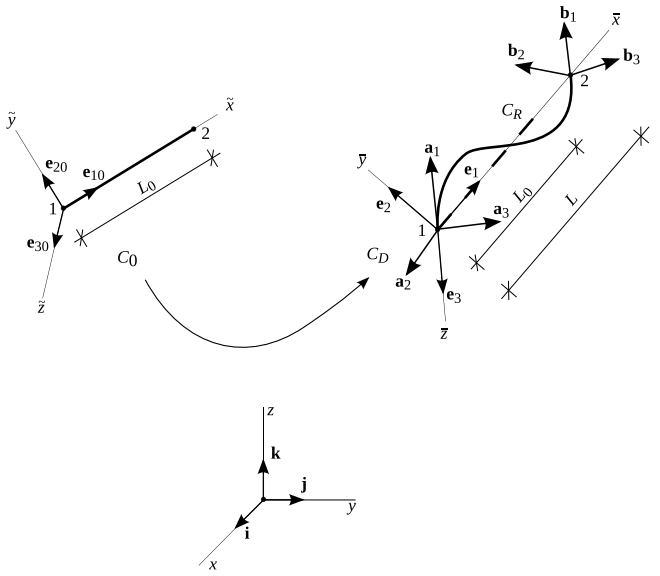

Fig. 7. Global, base, corotational and nodal systems.

refer to the base and corotational systems, respectively. Quantities without these symbols will refer to the global system. For instance, $\mathbf{x}_R$ denotes the position vector in the configuration C_R whose components are referred to the global system.

Hence, the orientation of the base system is defined as

$$\mathbf{e}_{10} = \frac{\mathbf{X}_{21}}{|\mathbf{X}_{21}|} \qquad \mathbf{e}_{30} = \frac{\mathbf{e}_{10} \times \mathbf{v}}{|\mathbf{e}_{10} \times \mathbf{V}|} \qquad \mathbf{e}_{20} = \mathbf{e}_{30} \times \mathbf{e}_{10} \tag{43}$$

where $\mathbf{X}_{21} = \mathbf{X}_2 - \mathbf{X}_1$, with $\mathbf{X}_i$ denoting the nodal coordinates in the global system of the element node i in the configuration C_0. The vector $\mathbf{v}$ is an auxiliary vector in the plane $\tilde{x}\tilde{y}$.

The motion of the finite element from the configuration C_0 to the deformed configuration C_D can be split into two parts (Fig. 8). First, the nodes 1 and 2 translate $\mathbf{u}_1$ and $\mathbf{u}_2$, respectively, deforming axially the element. Second, the nodal systems rotate θ_1 and θ_2 with respect to the configuration C_0 introducing bending and torsion. Therefore, in the configuration C_D, the position of the element nodes in the global system is given by

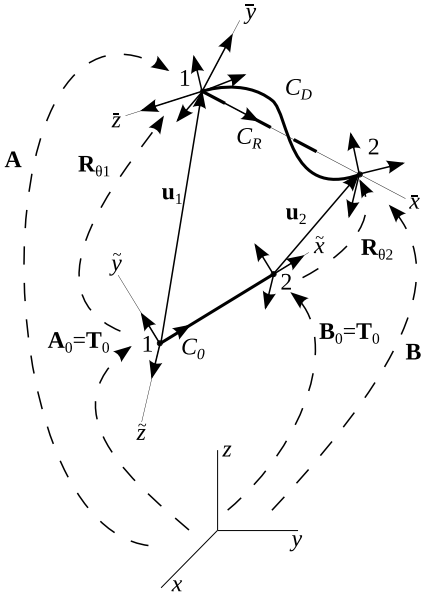

Fig. 8. Element motion.

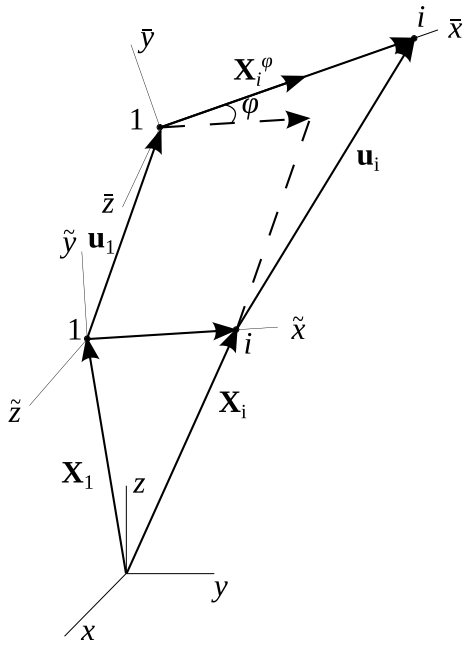

Fig. 9. Vector $\mathbf{X}_i^{\varphi}$.

$$\mathbf{x}_i = \mathbf{X}_i + \mathbf{u}_i \quad i = 1,2 \tag{44}$$

while the orientation of the nodal axes can be written as

$$\mathbf{A} = [\mathbf{a}_1 \;\; \mathbf{a}_2 \;\; \mathbf{a}_3] = \mathbf{R}_{\theta_1}\mathbf{A}_0 \qquad \mathbf{B} = [\mathbf{b}_1 \;\; \mathbf{b}_2 \;\; \mathbf{b}_3] = \mathbf{R}_{\theta_2}\mathbf{B}_0 \tag{45}$$

with $\mathbf{A}_0$ and $\mathbf{B}_0$ denoting $\mathbf{A}$ and $\mathbf{B}$ in the configuration C_0. Similar to the base system, the orientation of the corotational system $\bar{x}\bar{y}\bar{z}$ referred to the global system is given by

$$\mathbf{e}_1 = \frac{\mathbf{x}_{21}}{|\mathbf{x}_{21}|} \qquad \mathbf{e}_3 = \frac{\mathbf{e}_1 \times \mathbf{a}_2}{|\mathbf{e}_1 \times \mathbf{a}_2|} \qquad \mathbf{e}_2 = \mathbf{e}_3 \times \mathbf{e}_1. \tag{46}$$

Once the base and corotational systems are stated, then deformational displacements and rotations can be referred to the base system as follows. The corotational displacement $\bar{\mathbf{u}}_{Ri}$ of the i-th node can be computed as (Fig. 9)

$$\bar{\mathbf{u}}_{Ri} = \mathbf{T}^T(\mathbf{X}_{i1} + \mathbf{u}_i - \mathbf{u}_1) - \mathbf{X}_i^{\varphi} \tag{47}$$

where

$$\mathbf{X}_{i1} = \mathbf{X}_i - \mathbf{X}_1 \qquad \mathbf{X}_i^{\varphi} = |\mathbf{X}_{i1}|\,\bar{\mathbf{e}}_1 \tag{48}$$

and $\bar{\mathbf{e}}_1 = \{1 \;\; 0 \;\; 0\}^T$.

The global rotation θ_i is now split into two parts: one rigid part θ_p, which rotates with the element from configuration C_0 to configuration C_R, followed by the deformational part θ_{is}, which takes place from configuration C_R to C_D. The composition of these two rotations can be written as

$$\mathbf{R}_{\theta_i} = \mathbf{R}_{\theta_{is}}\mathbf{R}_{\theta_p} \tag{49}$$

where rigid body rotation is given by

$$\mathbf{R}_{\theta_p} = \mathbf{T}\mathbf{T}_0^T \tag{50}$$

and, thus,

$$\mathbf{R}_{\theta_{is}} = \mathbf{R}_{\theta_i}\mathbf{T}_0\mathbf{T}^T. \tag{51}$$

The corotational rotations can be obtained by the tensor transformation

$$\mathbf{R}_{\bar{\theta}_{Ri}} = \mathbf{T}^T\mathbf{R}_{\theta_{is}}\mathbf{T} = \mathbf{T}^T\mathbf{R}_{\theta_i}\mathbf{T}_0 \qquad \bar{\theta}_{Ri} = rot\left(\mathbf{R}_{\bar{\theta}_{Ri}}\right) \tag{52}$$

The corotational displacements are

$$\bar{\mathbf{d}}_R = \begin{Bmatrix} \bar{\mathbf{d}}_{R1} \\ \bar{\mathbf{d}}_{R2} \end{Bmatrix} \tag{53}$$

where

$$\bar{\mathbf{d}}_{R1} = \begin{Bmatrix} \bar{\mathbf{u}}_{R1} \\ \bar{\theta}_{R1} \end{Bmatrix} \qquad \bar{\mathbf{u}}_{R1} = \begin{Bmatrix} 0 \\ 0 \\ 0 \end{Bmatrix} \qquad \bar{\theta}_{R1} = rot\;\left(\mathbf{T}^T\mathbf{R}_{\theta_1}\mathbf{T}_0\right) = rot\;\left(\mathbf{T}^T\mathbf{A}\right) \tag{54}$$

and

$$\bar{\mathbf{d}}_{R2} = \begin{Bmatrix} \bar{\mathbf{u}}_{R2} \\ \bar{\theta}_{R2} \end{Bmatrix} \qquad \bar{\mathbf{u}}_{R2} = \begin{Bmatrix} L - L_0 \\ 0 \\ 0 \end{Bmatrix} \qquad \bar{\theta}_{R2} = rot\;\left(\mathbf{T}^T\mathbf{R}_{\theta_2}\mathbf{T}_0\right) = rot\;\left(\mathbf{T}^T\mathbf{B}\right). \tag{55}$$

The initial and current element lengths are identified as

$$L_0 = |\mathbf{X}_{21}| \qquad L = |\mathbf{x}_{21}|. \tag{56}$$

3.3. Global internal force vector and tangent stiffness matrix

Let $\mathbf{f}_D$ and $\bar{\mathbf{f}}_R$ be the internal force vectors referred to the global and corotational systems, respectively. Let $\mathbf{d}_D$ be the element nodal displacements between C_0 and C_D referred to the global system. As the virtual work done by the internal forces is invariant with respect to change of coordinate systems,

$$\delta\mathbf{d}_D^T\mathbf{f}_D = \delta\bar{\mathbf{d}}_R^T\bar{\mathbf{f}}_R. \tag{57}$$

In the corotational approach, before any computation at element level, the deformational part $\delta\bar{\mathbf{d}}_R$ is obtained purging the rigid body modes from the total displacement $\delta\mathbf{d}_D$. This pre-processing of nodal displacements can be performed out of the standard finite element routines. To perform this task, it is necessary to introduce the following relation

$$\delta\bar{\mathbf{d}}_R = \mathbf{P}\,\delta\bar{\mathbf{d}}_D \tag{58}$$

where $\delta\bar{\mathbf{d}}_R$ is $\delta\bar{\mathbf{d}}_D$ in the corotational system. The relationship between the variations of total displacements in the global and corotational systems is given by

$$\delta\bar{\mathbf{d}}_D = \mathbf{G}^T\delta\mathbf{d}_D \qquad \mathbf{G} = \begin{bmatrix} \mathbf{T} & \mathbf{0} & \mathbf{0} & \mathbf{0} \\ \mathbf{0} & \mathbf{T} & \mathbf{0} & \mathbf{0} \\ \mathbf{0} & \mathbf{0} & \mathbf{T} & \mathbf{0} \\ \mathbf{0} & \mathbf{0} & \mathbf{0} & \mathbf{T} \end{bmatrix}. \tag{59}$$

The matrix $\mathbf{P}$ has the property $\mathbf{P}^2 = \mathbf{P}$ and, therefore, is a projector matrix. In Equation (58), the matrix $\mathbf{P}$ acts like a filter extracting the body rigid modes from the vector $\delta\bar{\mathbf{d}}_D$. Substitution of Equations (58) and (59) into Equation (57), taking into account that $\delta\mathbf{d}_D$ is arbitrary, leads to

$$\mathbf{f}_D = \mathbf{G}\,\mathbf{P}^T\,\bar{\mathbf{f}}_R. \tag{60}$$

The tangent stiffness matrix

$$\mathbf{k}_D = \mathbf{G}\,\mathbf{P}^T\,\bar{\mathbf{k}}_R\,\mathbf{P}\,\mathbf{G}^T + \left.\frac{\partial(\mathbf{G}\,\mathbf{P}^T\bar{\mathbf{f}}_R)}{\partial\mathbf{d}_D}\right|_{\bar{\mathbf{f}}_R} \tag{61}$$

in global coordinates is obtained by differentiation of the internal force vector $\mathbf{f}_D$ with respect to the nodal displacements. The first term in this expression represents the elastic stiffness matrix and the second term corresponds to the geometric stiffness matrix.

Equations (60) and (61) as well as the terms $\mathbf{P}$ and $\partial(\mathbf{G}\,\mathbf{P}^T\bar{\mathbf{f}}_R)/\partial\mathbf{d}_D$ characterize the corotational formulation used in this work. It is important to emphasize that these equations are independent of the local element terms $\bar{\mathbf{f}}_R$ and $\bar{\mathbf{k}}_R$. Consequently, local elements with the same nodes and degrees of freedom share identical matrix transformations. In this sense, the above corotational approach is element independent [25], and the finite elements presented in Section 2 can be used as local elements ($\bar{\mathbf{f}}_R = \mathbf{g}$; $\bar{\mathbf{k}}_R = \mathbf{k}_t$).

3.4. Displacement update

The nonlinear equilibrium equations will be solved using the Newton-Raphson method. In this method, the nodal displacements are updated at each iteration k as

$$\mathbf{d}_{k+1} = \mathbf{d}_k + \delta\mathbf{d}_k. \tag{62}$$

Mathematically, this expression is consistent only for translational degrees of freedom, since space rotations are not additive. Therefore, the update of the nodal translations $\mathbf{u}$ is performed by

$$\mathbf{u}_{k+1} = \mathbf{u}_k + \delta\mathbf{u}_k \tag{63}$$

while the update of the nodal rotations θ can be properly performed using the rotation tensor [35].

$$\mathbf{R}_{\theta_{k+1}} = \mathbf{R}_{\delta\theta_k}\,\mathbf{R}_{\theta_k}. \tag{64}$$

For small rotation $\delta\theta$ [22],

$$\mathbf{R}_{\delta\theta} = \mathbf{I} + \mathbf{S}_{\delta\theta}. \tag{65}$$

Thus, for small iterative increments, the rotation tensor can be updated as follows:

- Substitution of Equation (65) into Equation (64):

$$\mathbf{R}_{\theta_{k+1}} = \mathbf{R}_{\theta_k} + \mathbf{S}_{\delta\theta_k}\,\mathbf{R}_{\theta_k}. \tag{66}$$

- Expansion of $\mathbf{R}_\theta$ in Taylor series and truncation at the linear term:

$$\mathbf{R}_{\theta_{k+1}} = \mathbf{R}_{\theta_k} + \delta\mathbf{R}_{\theta_k}. \tag{67}$$

3.5. Change of variables

Following Monteiro [35], a new rotation variable $\underset{\sim}{\theta}$ is defined so that the update expressed by Equation (66),

$$\underset{\sim k+1}{\mathbf{R}_{\theta}} = \underset{\sim k}{\mathbf{R}_{\delta\theta}}\,\underset{\sim k}{\mathbf{R}_{\theta}}, \tag{68}$$

be equal to the increment given by Equation (67):

$$\underset{\sim}{\mathbf{S}_{\delta\theta}} = \delta\mathbf{R}_\theta\,\mathbf{R}_\theta^T. \tag{69}$$

Using the concept of spatial and material rotations presented by Argyris [22], an expression similar to Equation (69) was obtained by Battini and Pacoste [26] and Pacoste and Eriksson [34]. Crisfield [33] also presented the same relationship using the sum of the vector (pseudovector) rotation components. It is important to note that the change of variables to instantaneous spin variables yields the commonly accepted interpretation of moments and forces [30].

The relationship between the rotations $\delta\theta$ and $\delta\underset{\sim}{\theta}$ reads [35].

$$\delta\theta = \boldsymbol{\Lambda}_\theta\,\delta\underset{\sim}{\theta} \qquad \boldsymbol{\Lambda}_\theta = \frac{\partial\theta}{\partial\underset{\sim}{\theta}} = \mathbf{I} - \frac{1}{2}\mathbf{S}_\theta + \xi\,\mathbf{S}_\theta^2$$
$$\xi = \frac{2\sin\theta - \theta(1+\cos\theta)}{2\theta^2\sin\theta}. \tag{70}$$

Once the nodal displacements and the rotation tensor have been updated, the generalized corotational displacements are evaluated from Equations (47) and (52). Using the adopted local tangent stiffness matrix $\bar{\mathbf{k}}_R$, one evaluates

$$\delta\bar{\mathbf{f}}_R = \bar{\mathbf{k}}_R\,\delta\bar{\mathbf{d}}_R \qquad \bar{\mathbf{f}}_R = \begin{Bmatrix}\bar{\mathbf{f}}_{R1}\\ \bar{\mathbf{f}}_{R2}\end{Bmatrix} \qquad \bar{\mathbf{f}}_{Ri} = \begin{Bmatrix}\bar{\mathbf{n}}_{Ri}\\ \bar{\mathbf{m}}_{Ri}\end{Bmatrix} \tag{71}$$

where $\bar{\mathbf{n}}_{Ri}$ and $\bar{\mathbf{m}}_{Ri}$ are the corotational forces at node i.

It is necessary to update $\bar{\mathbf{f}}_R$ and $\bar{\mathbf{k}}_R$ due to the change of variable of rotation. The vectors $\delta\bar{\mathbf{d}}_R$ and $\delta\underset{\sim}{\bar{\mathbf{d}}}_R$ are related by

$$\delta\bar{\mathbf{d}}_R = \frac{\partial\bar{\mathbf{d}}_R}{\partial\underset{\sim}{\bar{\mathbf{d}}}_R}\,\delta\underset{\sim}{\bar{\mathbf{d}}}_R = \mathbf{H}_R\,\delta\underset{\sim}{\bar{\mathbf{d}}}_R \tag{72}$$

where the matrix

$$\mathbf{H}_R = \frac{\partial\bar{\mathbf{d}}_R}{\partial\underset{\sim}{\bar{\mathbf{d}}}_R} = \begin{bmatrix}\mathbf{H}_{R_{11}} & \mathbf{H}_{R_{12}}\\ \mathbf{H}_{R_{21}} & \mathbf{H}_{R_{22}}\end{bmatrix} \qquad \mathbf{H}_{R_{ij}} = \frac{\partial\bar{\mathbf{d}}_{Ri}}{\partial\underset{\sim}{\bar{\mathbf{d}}}_{Rj}} = \begin{bmatrix}\frac{\partial\bar{\mathbf{u}}_{Ri}}{\partial\bar{\mathbf{u}}_{Rj}} & \frac{\partial\bar{\mathbf{u}}_{Ri}}{\partial\underset{\sim}{\bar{\theta}}_{Rj}}\\ \frac{\partial\bar{\theta}_{Ri}}{\partial\bar{\mathbf{u}}_{Rj}} & \frac{\partial\bar{\theta}_{Ri}}{\partial\underset{\sim}{\bar{\theta}}_{Rj}}\end{bmatrix}. \tag{73}$$

Using Equation (70),

$$\mathbf{H}_{R_{ij}} = \begin{bmatrix}\delta_{ij}\,\mathbf{I} & \mathbf{0}\\ \mathbf{0} & \delta_{ij}\,\frac{\partial\bar{\theta}_{Ri}}{\partial\underset{\sim}{\bar{\theta}}_{Rj}}\end{bmatrix} = \delta_{ij}\begin{bmatrix}\mathbf{I} & \mathbf{0}\\ \mathbf{0} & \boldsymbol{\Lambda}_{\bar{\theta}_{Ri}}\end{bmatrix} \tag{74}$$

where δ_{ij} is the Kronecker delta.

As the virtual work is invariant with respect to change of variables,

$$\delta\underset{\sim}{\bar{\mathbf{d}}}_R^T\,\underset{\sim}{\bar{\mathbf{f}}}_R = \delta\bar{\mathbf{d}}_R^T\,\bar{\mathbf{f}}_R, \tag{75}$$

one gets from Equations (71), (72) and (74)

$$\underset{\sim}{\bar{\mathbf{f}}}_R = \mathbf{H}_R^T\,\bar{\mathbf{f}}_R = \begin{Bmatrix}\bar{\mathbf{n}}_{R1}\\ \boldsymbol{\Lambda}_{\bar{\theta}_{R1}}^T\,\bar{\mathbf{m}}_{R1}\\ \bar{\mathbf{n}}_{R2}\\ \boldsymbol{\Lambda}_{\bar{\theta}_{R2}}^T\,\bar{\mathbf{m}}_{R2}\end{Bmatrix}. \tag{76}$$

The change of variable leads to the new local stiffness matrix

$$\underset{\sim}{\bar{\mathbf{k}}}_R = \frac{\partial\underset{\sim}{\bar{\mathbf{f}}}_R}{\partial\underset{\sim}{\bar{\mathbf{d}}}_R} = \mathbf{H}_R^T\frac{\partial\underset{\sim}{\bar{\mathbf{f}}}_R}{\partial\underset{\sim}{\bar{\mathbf{d}}}_R} + \frac{\partial}{\partial\underset{\sim}{\bar{\mathbf{d}}}_R}(\mathbf{H}_R^T\,\bar{\mathbf{f}}_R)_{\bar{\mathbf{f}}_R\,\text{constant}} = \underset{\sim}{\bar{\mathbf{k}}}_{R1} + \underset{\sim}{\bar{\mathbf{k}}}_{R2} \tag{77}$$

where

$$\underset{\sim}{\bar{\mathbf{k}}}_{R1} = \mathbf{H}_R^T\frac{\partial\underset{\sim}{\bar{\mathbf{f}}}_R}{\partial\underset{\sim}{\bar{\mathbf{d}}}_R} = \mathbf{H}_R^T\frac{\partial\underset{\sim}{\bar{\mathbf{f}}}_R}{\partial\bar{\mathbf{d}}_R}\frac{\partial\bar{\mathbf{d}}_R}{\partial\underset{\sim}{\bar{\mathbf{d}}}_R} = \mathbf{H}_R^T\,\underset{\sim}{\bar{\mathbf{k}}}_R\,\mathbf{H}_R \tag{78}$$

and

$$\underset{\sim}{\bar{\mathbf{k}}}_{R2} = \frac{\partial}{\partial\underset{\sim}{\bar{\mathbf{d}}}_R}(\mathbf{H}_R^T\,\bar{\mathbf{f}}_R)_{\bar{\mathbf{f}}_R\,\text{constant}} = \frac{\partial}{\partial\bar{\mathbf{d}}_R}(\mathbf{H}_R^T\,\bar{\mathbf{f}}_R)_{\bar{\mathbf{f}}_R\,\text{constant}}\frac{\partial\bar{\mathbf{d}}_R}{\partial\underset{\sim}{\bar{\mathbf{d}}}_R} = \frac{\partial}{\partial\bar{\mathbf{d}}_R}\begin{Bmatrix}\bar{\mathbf{n}}_{R1}\\ \boldsymbol{\Lambda}_{\bar{\theta}_{R1}}^T\,\bar{\mathbf{m}}_{R1}\\ \bar{\mathbf{n}}_{R2}\\ \boldsymbol{\Lambda}_{\bar{\theta}_{R2}}^T\,\bar{\mathbf{m}}_{R2}\end{Bmatrix}\mathbf{H}_R. \tag{79}$$

Note that the term $\partial(\mathbf{H}_R^T\,\bar{\mathbf{f}}_R)_{\bar{\mathbf{f}}_R\,\text{constant}}/\partial\bar{\mathbf{d}}_R$ is evaluated with $\bar{\mathbf{f}}_R$ kept constant. Thus,

$$\frac{\partial\bar{\mathbf{n}}_{R1}}{\partial\bar{\mathbf{d}}_R} = \frac{\partial\bar{\mathbf{n}}_{R2}}{\partial\bar{\mathbf{d}}_R} = \mathbf{0}_{3\text{x}12} \tag{80}$$

and

$$\frac{\partial}{\partial\bar{\mathbf{d}}_R}\left(\boldsymbol{\Lambda}_{\bar{\theta}_{R1}}^T\,\bar{\mathbf{m}}_{R1}\right) = [\mathbf{0}\quad\boldsymbol{\Omega}_{R1}\quad\mathbf{0}\quad\mathbf{0}] \qquad \boldsymbol{\Omega}_{R1} = \frac{\partial}{\partial\bar{\theta}_{R1}}\left(\boldsymbol{\Lambda}_{\bar{\theta}_{R1}}^T\,\bar{\mathbf{m}}_{R1}\right)$$
$$\frac{\partial}{\partial\bar{\mathbf{d}}_R}\left(\boldsymbol{\Lambda}_{\bar{\theta}_{R2}}^T\,\bar{\mathbf{m}}_{R2}\right) = [\mathbf{0}\quad\mathbf{0}\quad\mathbf{0}\quad\boldsymbol{\Omega}_{R2}] \qquad \boldsymbol{\Omega}_{R2} = \frac{\partial}{\partial\bar{\theta}_{R2}}\left(\boldsymbol{\Lambda}_{\bar{\theta}_{R2}}^T\,\bar{\mathbf{m}}_{R2}\right). \tag{81}$$

The above derivatives can be performed by [30,35].

$$\frac{\partial}{\partial\theta}(\boldsymbol{\Lambda}_\theta^T\,\mathbf{m}) = -\frac{1}{2}\mathbf{S}_m + \xi(\theta^T\,\mathbf{m}\,\mathbf{I} + \theta\,\mathbf{m}^T - 2\,\mathbf{m}\,\theta^T) + \mu\,\mathbf{S}_\theta^2\,\mathbf{m}\,\theta^T \tag{82}$$

where

$$\mu = \frac{1}{\theta}\frac{d\xi}{d\theta} = \frac{\theta(\sin\theta+\theta) - 8\sin^2(\theta/2)}{4\theta^2\sin(\theta/2)}. \tag{83}$$

Finally, substitution of Equations (80) and (81) into Equation (79) gives

$$\underset{\sim}{\bar{\mathbf{k}}}_{R2} = \boldsymbol{\Omega}_R \, \mathbf{H}_R \qquad \boldsymbol{\Omega}_R = \begin{bmatrix} \mathbf{0} & \mathbf{0} & \mathbf{0} & \mathbf{0} \\ \mathbf{0} & \boldsymbol{\Omega}_{R1} & \mathbf{0} & \mathbf{0} \\ \mathbf{0} & \mathbf{0} & \mathbf{0} & \mathbf{0} \\ \mathbf{0} & \mathbf{0} & \mathbf{0} & \boldsymbol{\Omega}_{R2} \end{bmatrix}. \tag{84}$$

It is important to note that the matrix $\underset{\sim}{\bar{\mathbf{k}}}_{R1}$, expressed in Equation (78), will be symmetric provided that the matrix $\underset{\sim}{\bar{\mathbf{k}}}_{R}$ is also symmetric. For local nonlinear finite elements, the dependency of $\underset{\sim}{\bar{\mathbf{k}}}_{R}$ on $\bar{\mathbf{d}}_R$ should be take into account in the evaluation of $\underset{\sim}{\bar{\mathbf{k}}}_{R1}$. On the other hand, the matrix $\underset{\sim}{\bar{\mathbf{k}}}_{R2}$, expressed in Equation (84), is not symmetric. Thus, the matrix $\underset{\sim}{\bar{\mathbf{k}}}_{R}$ with respect to the new rotation variable is not symmetric.

According to Monteiro [35], the matrix $\mathbf{H}_R$ tends to the identity matrix for small corotational rotations or when the mesh is refined. In this case, the unsymmetric matrix $\underset{\sim}{\bar{\mathbf{k}}}_{R2}$ can be neglected and $\underset{\sim}{\bar{\mathbf{k}}}_{R} = \underset{\sim}{\bar{\mathbf{k}}}_{R1}$ for practical purposes. Since this issue is not the focus of the present work, the full non-symmetric matrix will be adopted in all calculations.

Due to the change of variable, the expression (58) takes the form

$$\delta\underset{\sim}{\bar{\mathbf{d}}}_{R} = \underset{\sim}{\mathbf{P}} \, \delta\underset{\sim}{\bar{\mathbf{d}}}_{D} \tag{85}$$

where details on the development of the new projector matrix $\underset{\sim}{\mathbf{P}}$ are in Appendix A.

3.6. Internal force vector and tangent stiffness matrix due to change of variables

From the virtual work statement

$$\delta\underset{\sim}{\bar{\mathbf{d}}}_{D}^{T} \underset{\sim}{\bar{\mathbf{f}}}_{D} = \delta\underset{\sim}{\bar{\mathbf{d}}}_{R}^{T} \underset{\sim}{\bar{\mathbf{f}}}_{R} = \delta\underset{\sim}{\bar{\mathbf{d}}}_{D}^{T} \underset{\sim}{\mathbf{P}}^{T} \underset{\sim}{\bar{\mathbf{f}}}_{R} \tag{86}$$

one can write

$$\underset{\sim}{\bar{\mathbf{f}}}_{D} = \underset{\sim}{\mathbf{P}}^{T} \underset{\sim}{\bar{\mathbf{f}}}_{R}. \tag{87}$$

Substituting the projector matrix (A.9),

$$\underset{\sim}{\bar{\mathbf{f}}}_{D} = (\mathbf{I}_{12} - \boldsymbol{\Psi}\boldsymbol{\Gamma})^T \underset{\sim}{\bar{\mathbf{f}}}_{R} - \boldsymbol{\Phi}^T \underset{\sim}{\bar{\mathbf{f}}}_{R} \tag{88}$$

where the matrices $\mathbf{I}_{12}$, $\boldsymbol{\Psi}$ and $\boldsymbol{\Gamma}$ are defined in Equation (A.10).

The last term on the right-hand side of the above equation is

$$\boldsymbol{\Phi}^T \underset{\sim}{\bar{\mathbf{f}}}_{R} = \begin{bmatrix} \mathbf{I} & \mathbf{0} & \mathbf{I} & \mathbf{0} \\ \mathbf{0} & \mathbf{0} & \mathbf{0} & \mathbf{0} \\ \mathbf{0} & \mathbf{0} & \mathbf{0} & \mathbf{0} \\ \mathbf{0} & \mathbf{0} & \mathbf{0} & \mathbf{0} \end{bmatrix} \begin{Bmatrix} \bar{\mathbf{n}}_{R1} \\ \underset{\sim}{\bar{\mathbf{m}}}_{R1} \\ \bar{\mathbf{n}}_{R2} \\ \underset{\sim}{\bar{\mathbf{m}}}_{R2} \end{Bmatrix} = \begin{Bmatrix} \bar{\mathbf{n}}_{R1} + \bar{\mathbf{n}}_{R2} \\ \mathbf{0} \\ \mathbf{0} \\ \mathbf{0} \end{Bmatrix}. \tag{89}$$

Since the element is locally in equilibrium, then $\bar{\mathbf{n}}_{R1} + \bar{\mathbf{n}}_{R2} = 0$. Thus, Equation (87) reduces to

$$\underset{\sim}{\bar{\mathbf{f}}}_{D} = {}^{*}\underset{\sim}{\mathbf{P}}^{T} \underset{\sim}{\bar{\mathbf{f}}}_{R} \tag{90}$$

where ${}^{*}\mathbf{P}$

$${}^{*}\underset{\sim}{\mathbf{P}} = \mathbf{I}_{12} - \boldsymbol{\Psi}\boldsymbol{\Gamma} \tag{91}$$

Such an operator has also the property ${}^{*}\underset{\sim}{\mathbf{P}}^2 = {}^{*}\underset{\sim}{\mathbf{P}} \, {}^{*}\underset{\sim}{\mathbf{P}}^T$.

Equation (85) can now be replaced by

$$\delta\underset{\sim}{\bar{\mathbf{d}}}_{R} = {}^{*}\underset{\sim}{\mathbf{P}} \, \delta\underset{\sim}{\bar{\mathbf{d}}}_{D}. \tag{92}$$

Based on

$$\delta\underset{\sim}{\bar{\mathbf{d}}}_{D} = \mathbf{G}^T \, \delta\underset{\sim}{\mathbf{d}}_{D}, \tag{93}$$

the internal force vector reads

$$\underset{\sim}{\mathbf{f}}_{D} = \mathbf{G} \, \underset{\sim}{\bar{\mathbf{f}}}_{D} = \mathbf{G} \, {}^{*}\underset{\sim}{\mathbf{P}}^{T} \underset{\sim}{\bar{\mathbf{f}}}_{R}. \tag{94}$$

The element tangent stiffness matrix $\underset{\sim}{\mathbf{k}}_{D}$ is obtained from the variation

$$\delta\underset{\sim}{\mathbf{f}}_{D} = \delta\underset{\sim}{\mathbf{f}}_{D1} + \delta\underset{\sim}{\mathbf{f}}_{D2} + \delta\underset{\sim}{\mathbf{f}}_{D3} = \underset{\sim}{\mathbf{k}}_{D} \delta\underset{\sim}{\mathbf{d}}_{D} \tag{95}$$

For each element:

1. Computation of $\bar{\mathbf{d}}_R$ (Eq. (53)):
   (a) Compute $\mathbf{T}$ and $\mathbf{R}_{\theta_i}$
   (b) $\bar{\mathbf{u}}_{Ri} = \mathbf{T}^T (\mathbf{X}_{i1} + \mathbf{u}_i - \mathbf{u}_1) - \mathbf{X}_i^{\varphi}$
   (c) $\mathbf{R}_{\bar{\theta}_{R_i}} = \mathbf{T}^T \mathbf{R}_{\theta_i} \mathbf{T}_0$
   (d) $\bar{\boldsymbol{\theta}}_{Ri} = rot\left(\mathbf{R}_{\bar{\theta}_{Ri}}\right)$
2. Evaluation of the local internal force vector $\underset{\sim}{\bar{\mathbf{f}}}_{R}$ (Eq. (76)) and of the local stiffness matrix $\underset{\sim}{\bar{\mathbf{k}}}_{R}$ (Eq. (77)):
   (a) Evaluate constitutive matrix $\mathbf{C}_b$
   (b) Compute $\underset{\sim}{\bar{\mathbf{f}}}_{R}$ and $\underset{\sim}{\bar{\mathbf{k}}}_{R}$ (Section 2)
   (c) Compute $\mathbf{H}_R$ and its derivatives
3. Computation of the internal force vector $\underset{\sim}{\mathbf{f}}_{D}$:
   (a) Compute $\boldsymbol{\Psi}$ (Eq. (A.10)) and $\boldsymbol{\Gamma}$ (Eq. (A.12)) from $\mathbf{x}_{21}$, $\mathbf{R}_{\theta_1}$ and $\mathbf{T}_0$
   (b) Compute ${}^{*}\underset{\sim}{\mathbf{P}} = \mathbf{I}_{12} - \boldsymbol{\Psi}\boldsymbol{\Gamma}$ (Eq. (91))
   (c) Compute $\underset{\sim}{\bar{\mathbf{f}}}_{D} = {}^{*}\underset{\sim}{\mathbf{P}}^{T} \underset{\sim}{\bar{\mathbf{f}}}_{R}$ (Eq. (90))
   (d) Transform $\underset{\sim}{\bar{\mathbf{f}}}_{D}$ to the global coordinate system: $\underset{\sim}{\mathbf{f}}_{D} = \mathbf{G} \, \underset{\sim}{\bar{\mathbf{f}}}_{D} = \mathbf{G} \, {}^{*}\underset{\sim}{\mathbf{P}}^{T} \underset{\sim}{\bar{\mathbf{f}}}_{R}$ (Eq. (94))
4. Computation of the stiffness matrix $\underset{\sim}{\mathbf{k}}_{D}$:
   (a) Assemble $\mathbf{H}_1$ (Eq. (B.9)) and $\mathbf{H}_2$ (Eq. (B.12)) from $\underset{\sim}{\bar{\mathbf{f}}}_{D}$
   (b) $\underset{\sim}{\bar{\mathbf{k}}}_{D} = {}^{*}\underset{\sim}{\mathbf{P}}^{T} \underset{\sim}{\bar{\mathbf{k}}}_{R} \, {}^{*}\underset{\sim}{\mathbf{P}} - \boldsymbol{\Gamma}^T \mathbf{H}_1^T \, {}^{*}\underset{\sim}{\mathbf{P}} - \boldsymbol{\Upsilon} - \mathbf{H}_2 \boldsymbol{\Gamma}$ (Eq. (97))
   (c) Transform $\underset{\sim}{\bar{\mathbf{k}}}_{D}$ to the global coordinate system: $\underset{\sim}{\mathbf{k}}_{D} = \mathbf{G} \, \underset{\sim}{\bar{\mathbf{k}}}_{D} \, \mathbf{G}^T$ (Eq. (97))

Fig. 10. Corotational framework.

where

$$\delta\underset{\sim}{\mathbf{f}}_{D1} = \mathbf{G} \, {}^{*}\underset{\sim}{\mathbf{P}}^{T} \, \delta\underset{\sim}{\bar{\mathbf{f}}}_{R} \qquad \delta\underset{\sim}{\mathbf{f}}_{D2} = \mathbf{G} \, \delta{}^{*}\underset{\sim}{\mathbf{P}}^{T} \underset{\sim}{\bar{\mathbf{f}}}_{R} \qquad \delta\underset{\sim}{\mathbf{f}}_{D3} = \delta\mathbf{G} \, {}^{*}\underset{\sim}{\mathbf{P}}^{T} \underset{\sim}{\bar{\mathbf{f}}}_{R}. \tag{96}$$

The development of $\delta\underset{\sim}{\mathbf{f}}_{Di}$ given in Appendix B yields

$$\underset{\sim}{\mathbf{k}}_{D} = \mathbf{G} \, \underset{\sim}{\bar{\mathbf{k}}}_{D} \, \mathbf{G}^T \qquad \underset{\sim}{\bar{\mathbf{k}}}_{D} = {}^{*}\underset{\sim}{\mathbf{P}}^{T} \underset{\sim}{\bar{\mathbf{k}}}_{R} \, {}^{*}\underset{\sim}{\mathbf{P}} - \boldsymbol{\Gamma}^T \mathbf{H}_1^T \, {}^{*}\underset{\sim}{\mathbf{P}} - \boldsymbol{\Upsilon} - \mathbf{H}_2 \boldsymbol{\Gamma} \tag{97}$$

with the matrices $\mathbf{H}_1$ and $\boldsymbol{\Upsilon}$ defined in Equation (B.9) and $\mathbf{H}_2$ in Equation (B.12). The matrix $\boldsymbol{\Upsilon}$ is usually neglected in Equation (97) [30,32]. It is important to note that the matrix $\underset{\sim}{\bar{\mathbf{k}}}_{D}$ is not symmetric.

3.7. Computational aspects

The element independent corotational algorithm is summarized in Fig. 10. The first step filters the local (i.e. deformational) displacements and rotations from the total displacements and rotations. Step 2 computes the local internal force vector and local stiffness matrix (CRL and CRTL elements) using the deformation quantities evaluated in Step 1. Steps 3 and 4 involve computing the internal force vector and stiffness matrix and transforming them to the global coordinate system to solve the equilibrium equations.

The computer implementation is carried out in an open source software, written in C++ using an Object-Oriented Approach. Since the stiffness matrix is not symmetric, an appropriate skyline solver for non-symmetric matrices based on the LU decomposition is adopted to solve the global system of equations at each Newton-Raphson iteration to ensure the expected quadratic convergence rate.

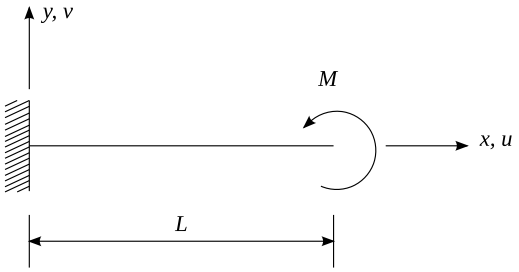

Fig. 11. Cantilever beam subjected to a moment M at the free end.

4. Numerical examples

The numerical examples in this section were analyzed using the Newton-Raphson method under load control [21]. Both isotropic and laminated composite beams will be considered, with $\mathbf{C}_b$ evaluated according to Section 2.1. The obtained results from both CRL and CRTL formulations will be compared with those available in the literature or evaluated using finite element models constructed with ABAQUS S8R shell elements based on Reissner-Mindlin assumptions [40].

4.1. Cantilever beam with end moment

In spite of its simple geometry and loading, the cantilever beam subjected to a moment at the free end shown in Fig. 11 represents a challenge to most beam formulations due to the presence of large rotations and inextensional bending.

Initially an isotropic beam of length $L = 3.2$ m, rectangular cross-section with width $b = 0.1$ m and height $h = 0.1$ m, and Young's modulus $E = 210$ GPa will be analyzed. The exact solution for the tip displacements is

$$\frac{u}{L} = \frac{\sin\theta}{\theta} - 1 \quad \frac{v}{L} = \frac{1-\cos\theta}{\theta} \quad \theta = \frac{ML}{EI} \tag{98}$$

where θ is the beam rotation about the z axis at the tip.

Two different meshes with 4 and 8 elements (CRL and CRTL) are considered. The results obtained are compared with the exact solution in Figs. 12 and 13. The load $M = 4\pi\, EI/L$, at which the beam is bent into two concentric circles, is applied at 20 equal increments. The equilibrium paths show that the finite element results are in very good agreement with the exact solution. Both elements yield good results for the finer mesh, but the CRTL element is more accurate for the coarse mesh.

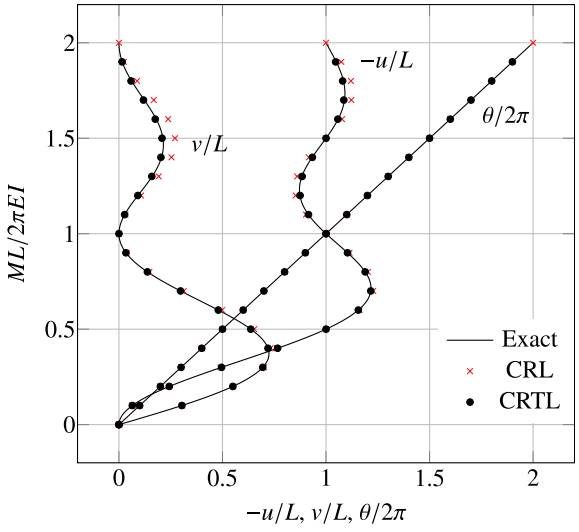

Fig. 12. Tip displacements for the isotropic beam with end moment and 4-element mesh.

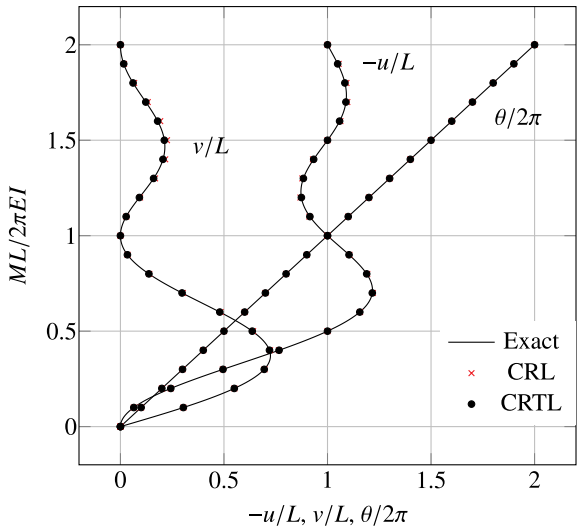

Fig. 13. Tip displacements for the isotropic beam with end moment and 8-element mesh.

Table 1
Tip displacements for $M = \pi EI/L$.

	v/L	$-u/L$	NE
Exact	0.6366	1.0000	–
Saravia et al. [5]	0.6339	1.0081	10
	0.6313	1.0081	50
Saravia et al. [7]	0.6222	1.0252	10
	0.6311	1.0088	50
CRL	0.6533	0.9999	4
	0.6407	1.0000	8
CRTL	0.6365	0.9999	4
	0.6366	0.9999	8

NE: number of elements.

Table 1 compares the results with those found in Ref. [5,7] at load $M = \pi EI/L$ which bends the beam into a semicircle. Once again, excellent results are obtained for both elements, with CRTL showing a better accuracy for the vertical displacements. The proposed elements lead to more accurate results, even using coarser meshes.

The beam of Fig. 11 is now treated as a 6-layer $[45/-45/45]_S$ laminated beam, with $L = 15$ m, $b = 0.15$ m, $h = 0.015$ m and plies of carbon/epoxy AS4/3501-6 with properties [41]: $E_{11} = 147.0$ GPa, $E_{22} = 10.3$ GPa, $G_{12} = 7.0$ GPa, $G_{23} = 3.7$ GPa and $\nu_{12} = 0.27$. The cross-section constitutive matrix is

$$\mathbf{C}_b = \begin{bmatrix} 5.3087\times10^7 & 0 & 0 & 0 \\ 0 & 1.0087\times10^3 & 0 & -4.0766\times10^2 \\ 0 & 0 & 9.9538\times10^4 & 0 \\ 0 & -4.0766\times10^2 & 0 & 5.4711\times10^3 \end{bmatrix}. \tag{99}$$

This matrix shows that this angle-ply layup leads to a bending-torsion coupling.

An end moment $M = 405$ Nm is applied at 20 equal increments and the beam is discretized with 4 and 8 elements CRL and CRTL. Since no exact solution is available, our results are compared with those obtained with a fine mesh of ABAQUS S8R elements with 2910 degrees of freedom (2 elements in the section and 60 elements along the beam). As $\mathbf{C}_b$ is not diagonal, an exact bending stiffness $\overline{EI}$ cannot be defined, but a good approximation can be computed as $\overline{EI} = 1/\mathbf{S}_b(2,2)$ where $\mathbf{S}_b = \mathbf{C}_b^{-1}$. The obtained value is $\overline{EI} = 978.34$ Nm^2 and it is used to normalize the results presented in Figs. 14 and 15.

These figures show that an excellent agreement is found with 4- and

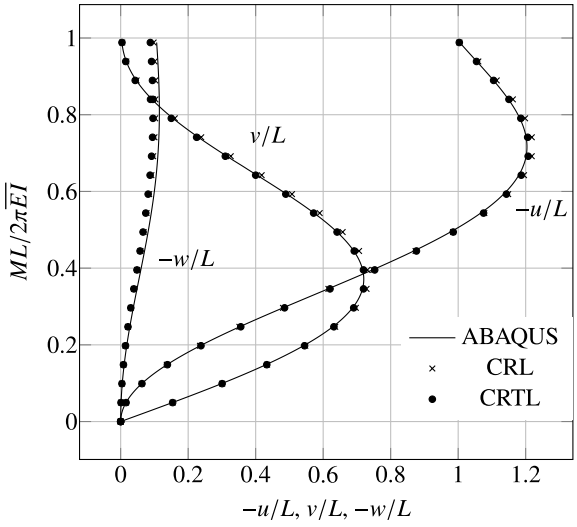

Fig. 14. Tip displacements for the laminated beam with end moment and 4-element mesh.

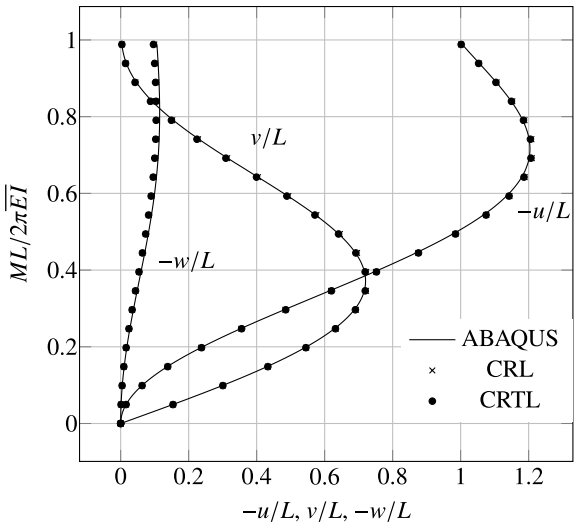

Fig. 15. Tip displacements for the laminated beam with end moment and 8-element mesh.

8-element meshes for both displacements u and v regardless of the load level. It can also be noted that there is out of plane displacement w due to the bending-torsion coupling induced by the composite layup, which does not occurs for isotropic beams.

4.2. Cantilever beam with transverse end load

In this second example, the isotropic cantilever beam with $L = 3.2$ m, $b = 0.1$ m, $h = 0.1$ m and $E = 210$ GPa, analyzed in the previous example, is supposed to be subjected to a tip load F as shown in Fig. 16.

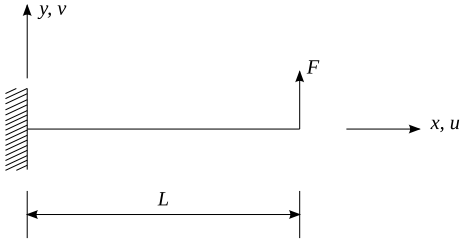

Fig. 16. Cantilever beam with transverse end load.

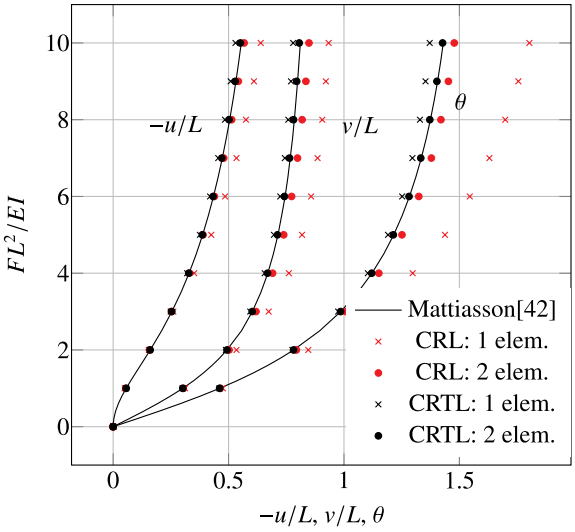

Fig. 17. Tip displacements for the isotropic beam with transverse end load.

Meshes with 1 and 2 CRL and CRTL elements are adopted and the results obtained are compared with those found in Mattiasson [42]. The displacements u, v and rotation θ at the free end are shown in Fig. 17 for the load $F = 10EI/L^2$ applied at 10 equal increments.

Both elements yielded good results, especially when 2-element mesh is used. Once again, the results of CRTL element are more accurate than those of CRL, due to the consideration of the geometric nonlinearity in the local level. Based on these results, only the CRTL element will be used in the next analyses.

Two different laminated beams are now considered: a tube and a box beam of lengths $L = 6$ m and $L = 7$ m, respectively. The tube has mean radius $R = 60$ mm and the box beam has $b = 50$ mm and $d = 70$ mm, as depicted in Fig. 18. Both have a 6-layer of carbon/epoxy AS4/3501-6 and thickness $h = 1$ mm. A symmetric angle-ply layup $[45/-45/45]_S$ laminated beam is adopted for the tube and a non-symmetric angle-ply layup $[0/90/-45/0/90/-45]$ for the box beam. The material properties are the same of the first example.

The cross-section constitutive matrix for the laminated tube is

$$\mathbf{C}_b = \begin{bmatrix} 5.4084 \times 10^7 & 0 & 0 & -4.5396 \times 10^5 \\ 0 & 9.6145 \times 10^4 & 0 & 0 \\ 0 & 0 & 9.6145 \times 10^4 & 0 \\ -4.5396 \times 10^5 & 0 & 0 & 2.8925 \times 10^5 \end{bmatrix} \tag{100}$$

and for the laminated box beam this matrix is

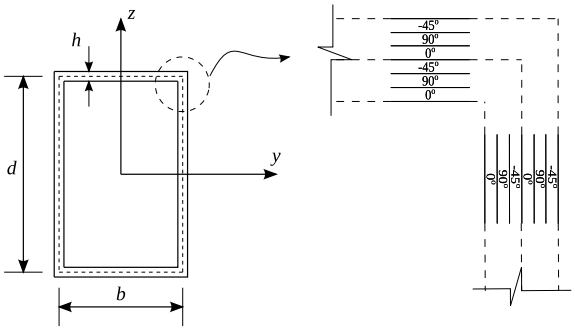

Fig. 18. Box beam dimensions and stacking sequence.

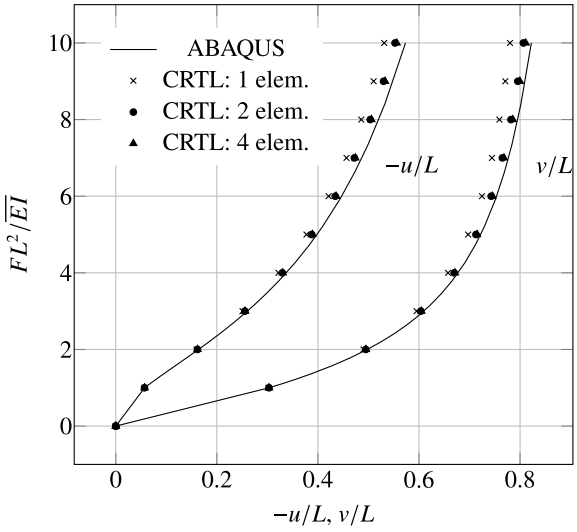

Fig. 19. Tip displacements for the laminated tube with transverse end load.

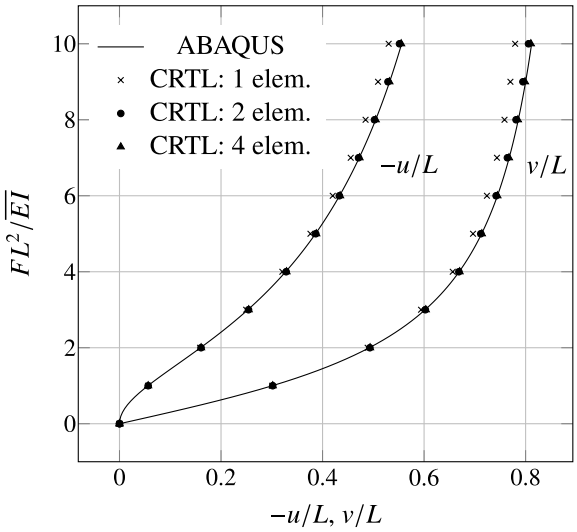

Fig. 20. Tip displacements for the laminated box beam with transverse end load.

$$\mathbf{C}_b = \begin{bmatrix} 9.5258 \times 10^7 & 0 & 0 & -3.6202 \times 10^5 \\ 0 & 6.3687 \times 10^4 & 0 & 0 \\ 0 & 0 & 3.7809 \times 10^4 & 0 \\ -3.6202 \times 10^5 & 0 & 0 & 1.7834 \times 10^4 \end{bmatrix}. \tag{101}$$

Therefore, both composite beams present extension-torsion coupling.

Similar to the isotropic cantilever beam, a load $F = 10\overline{EI}/L^2$ is applied at 10 equal increments. A linear analysis using a fine mesh of ABAQUS S8R elements is performed to evaluate the equivalent bending stiffness $\overline{EI} = PL^3 / (3v_{FEM})$, as stated by the classical Euler-Bernoulli-Navier theory, where v_{FEM} is the tip displacement [43]. Therefore, the loads $F = 26.8671$ kN and $F = 13.0064$ kN are used for the tube and box beam, respectively. In order to avoid local effects in the finite element results when the load F is applied at two points of the end section, the beam is made 1 mm longer using a rigid isotropic material ($E = 20000$ GPa and $\nu = 0.27$) before the load application.

The tube and box beam are discretized with 1, 2 and 4 CRTL elements and the results for displacements u and v at the free end are compared with those obtained with fine meshes of ABAQUS S8R elements with 103560 degrees of freedom in Fig. 19 and 103904 degrees of freedom in Fig. 20, respectively. A total of 5740 elements were used for the tube (20 in the section and 287 along the beam) and 7476 elements for the box (28 in the section and 267 along the beam). As can be seen, a good agreement is obtained using only 4 beam elements.

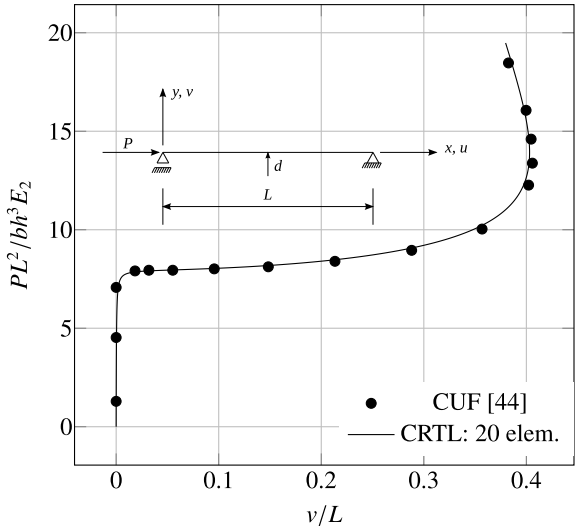

Fig. 21. Post-buckling equilibrium curves.

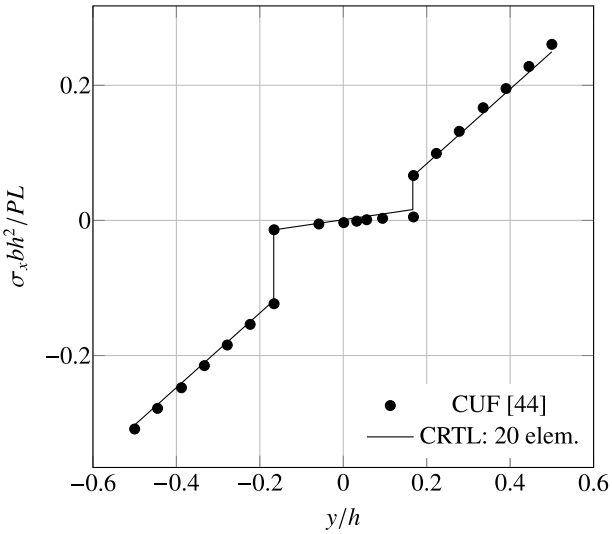

Fig. 22. Distribution of axial stress σ_x through the thickness of the cross-section at $x = 0.1L$ for $PL^2/bh^3E_2 = 8.12$.

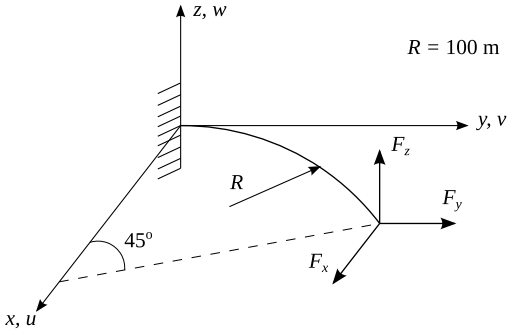

Fig. 23. 45-degree curved beam with end load.

Table 2
Tip displacements of the 45-degree curved beam.

Load	F_z = 300 N			F_z = 450 N			F_z = 600 N		
Works	u (m)	v (m)	w (m)	u (m)	v (m)	w (m)	u (m)	v (m)	w (m)
Bathe and Bolourchi [45]	−6.79	−11.51	39.50	–	–	–	−13.39	−23.50	53.40
Simo and Vu-Quoc [46]	−6.96	−11.87	40.08	−10.67	−18.39	48.39	−13.50	−23.48	53.37
Crisfield [31]	−7.13	−12.18	40.53	−10.86	−18.78	48.79	−13.68	−23.87	53.71
CRTL	−7.14	−12.14	40.47	−10.88	−18.70	48.72	−13.70	−23.78	53.64

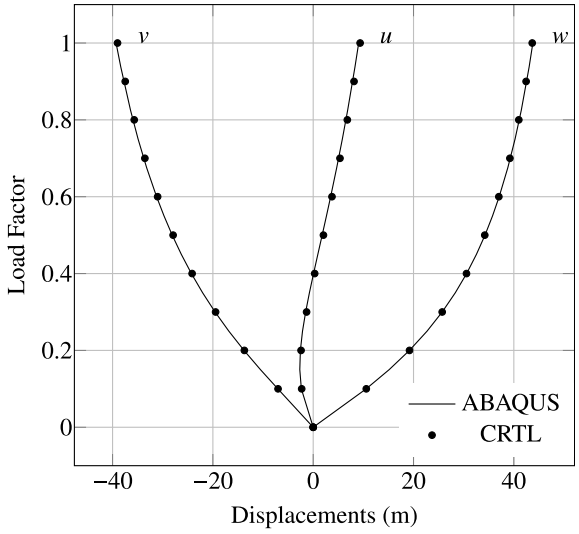

Fig. 24. Tip displacements for the laminated 45-degree curved beam with end load and 8-element mesh.

4.3. Post-buckling of symmetric cross-ply beam

This example corresponds to the post-buckling analysis of the symmetric cross-ply [0/90] beam shown in Fig. 21. This structure was previously analyzed by Pagani and Carrera [44] using the Carrera Unified Formulation (CUF) which employs Green-Lagrange terms within a total Lagragian framework along with a layerwise formulation. Good agreement was reported with respect to solutions of ABAQUS solid, shell and beam finite elements.

The beam length is $L = 250$ mm and the cross-section has $b = h =$ 5 mm. Each layer of the laminate has the same thickness ($t = h/3$) and orthotropic material with the following characteristics: $E_1 = 155.0$ GPa, $E_2 = 15.5$ GPa, $G_{12} = G_{13} = 0.6E_2$, $G_{23} = 0.5E_2$ and $\nu_{12} = 0.25$. It is worth emphasizing that a such layup gives rise to a diagonal constitutive matrix ($C_{11} = 2.7235 \times 10^6$, $C_{22} = 7.8148$, $C_{33} = 5.6739$, $C_{44} = 1.9375$).

A small perturbation load $d = 0.2$ N is applied as in Fig. 21 to enforce the stable branch after the buckling load has reached. The load $P = 155$ N was applied at equal increments. A mesh of 20 CRTL elements was adopted and results are compared with CUF beam model.

The nonlinear equilibrium curves are shown in Fig. 21 in which the vertical displacement component at the midspan section is given as function of the applied load P. A very good agreement is obtained between the proposed element and the CUF theory, even in the post-buckling range with very large displacements and rotations.

Fig. 22 shows the axial stress distribution along the thickness of the laminated beam at $x = 0.1L$ and load level $PL^2/bh^3E_2 = 8.12$, corresponding to a point in the nonlinear range. The stress in the laminate is computed using the procedure described in Section 2.1 based on the beam generalized forces. It can be noted that stresses computed with the proposed elements are in very good agreement with those obtained by the CUF model.

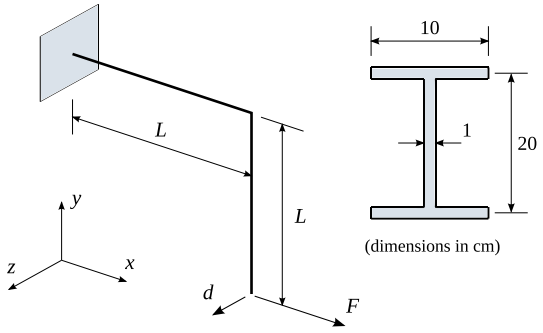

Fig. 25. Clamped right-angle frame with in-plane tip load.

4.4. A 45-degree curved beam with end load

The problem of a curved cantilever beam lying in the xy plane, as depicted in Fig. 23, was introduced by Bathe and Bolourchi [45]. They used solid and space frame elements, based on total and update Lagrangian descriptions, in the analysis of this structure under large rotations. The beam has length $\pi R/4$ with $R = 100$ m and a square cross-section of side 1.0 m. The isotropic material adopted has Young's modulus $E = 10$ MPa and Poisson's ratio $\nu = 0$.

The beam subdivided into 8 CRTL elements is subjected to a vertical load $F_z = 600$ N ($F_x = F_y = 0$) applied at 4 equal increments. Comparison of the obtained tip displacements u, v and w for load levels 300 N, 450 N and 600 N is made with available results in Table 2 to highlight the element precision.

A 4-layer $[45/-45]_S$ laminated box beam with square cross-section of side 1.0 m is now considered [7]. Each ply is 0.025 m thick and the material properties are $E_{11} = 45.0$ GPa, $E_{22} = 12.0$ GPa, $G_{12} = G_{23} = 5.5$ GPa and $\nu_{12} = 0.3$. This configuration leads to diagonal constitutive matrix ($C_{11} = 6.5945 \times 10^9$, $C_{22} = 1.1018 \times 10^9$, $C_{33} = 1.1018 \times 10^9$, $C_{44} = 1.2926 \times 10^9$).

The beam is subject to the loads $F_x = 4.0 \times 10^5$, $F_y = -4.0 \times 10^5$, $F_z = 8.0 \times 10^5$ applied at 10 equal increments. The results for an 8-CRTL element model are in excellent agreement with those obtained with a fine mesh of ABAQUS S8R elements with 2856 degrees of freedom (a total of 156 elements), as shown in Fig. 24.

4.5. Lateral buckling of right-angle frame

The last example is the clamped right-angle frame problem of Fig. 25, lying in the xy plane and subjected to an in-plane tip load. The frame legs have length $L = 4$ m and I cross-section with web in the plane xy of the frame. The I-section, whose geometry is shown in the figure, has web and flanges as being 4-layer $[\alpha/-\alpha]_S$ laminates. The material properties of the orthotropic laminae is given by $E_{11} = 133.4$ GPa, $E_{22} = 8.78$ GPa, $G_{12} = 3.67$ GPa and $\nu_{12} = 0.26$. This problem has also been studied by Lanc et al. [47] in the post-critical domain.

The cross-section constitutive matrix associated with $\alpha = 30°$ is

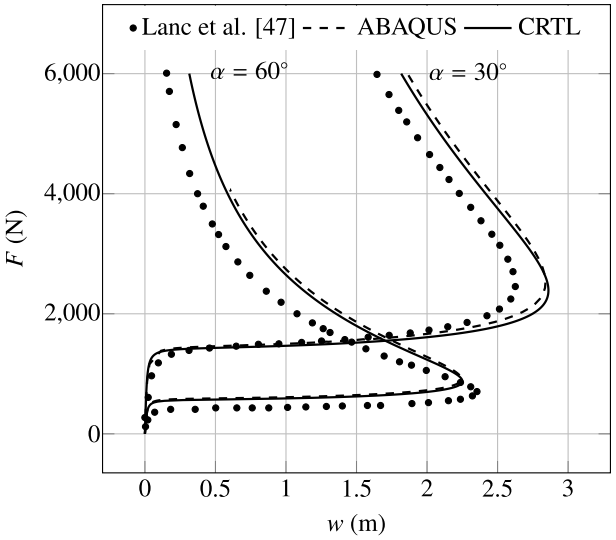

Fig. 26. Tip force F versus out-of-plane tip displacement w in the z direction for 4 CRTL elements per frame leg.

$$\mathbf{C}_b = \begin{bmatrix} 1.6517 \times 10^8 & 0 & 0 & 0 \\ 0 & 1.1019 \times 10^6 & 0 & 0 \\ 0 & 0 & 6.9511 \times 10^4 & 4.9640 \times 10^2 \\ 0 & 0 & 4.9640 \times 10^2 & 2.7442 \times 10^3 \end{bmatrix} \tag{102}$$

and with $\alpha = 60°$ is

$$\mathbf{C}_b = \begin{bmatrix} 3.5196 \times 10^7 & 0 & 0 & 0 \\ 0 & 2.3479 \times 10^5 & 0 & 0 \\ 0 & 0 & 1.4812 \times 10^4 & 1.9278 \times 10^1 \\ 0 & 0 & 1.9278 \times 10^1 & 2.0332 \times 10^3 \end{bmatrix}. \tag{103}$$

These matrices present bending-torsion coupling and show how the fiber orientation influences the magnitude of the terms in the cross-section constitutive matrix.

Using a mesh of 4 CRTL elements per frame leg, our results for lamina fiber orientation $\alpha = 30°$ and $\alpha = 60°$ are compared in Fig. 26 with those of Lanc et al. [47] and a model of ABAQUS S8R elements with 14742 degrees of freedom (a total of 768 elements: 4 for each flange and 4 for the web in the section, and 64 along the frame). The load $F = 6000$ N was applied at equal increments. As in the third example, a small perturbation tip load $d = 0.001F$ was applied in the z-direction to enforce the stable branch after the buckling load has reached. It is clear that the proposed corotational finite element model is in remarkably agreement with ABAQUS shell element results.

5. Conclusion

This paper presented two three-dimensional beam elements for nonlinear analysis of thin-walled laminated composite space frames based on the use of a fully coupled cross-sectional constitutive matrix, allowing the consideration of arbitrary layups. Thus, different couplings between generalized stress and strain can be considered. In the local system, one element is linearly formulated while the other incorporates moderate rotations. The corotational approach is used to handle large space rotations. The resulting tangent stiffness matrix is unsymmetric and a proper solver was used in order to preserve the quadratic convergence rate of the Newton-Raphson method.

Several numerical examples were analyzed to evaluate the performance of the proposed elements. The examples include composite beams with symmetric and non-symmetric layups leading to complex interactions between generalized stresses and strains, including extension-torsion and bending-torsion couplings. Both elements yield good results for isotropic and laminated beams with different cross-sections and composite layups. However, the CRTL element with geometric nonlinearity in the local level is more accurate, allowing the use of coarser meshes. This element was also successfully applied to the post-buckling analysis of laminated composite structures.

The CRTL element seems to be an excellent analysis tool for laminated composite beams with large rotations, since it simplifies the mesh generation and leads to a much lower cost than the use of shell elements, which is the standard approach to the analysis of laminated structures with arbitrary layups.

Finally, the methodology presented in Section 2 for stress computation based on the generalized forces from nonlinear solution leads to accurate stress/strain field through the thickness of cross-section.

Acknowledgements

The authors are grateful to CNPq (Conselho Nacional de Desenvolvimento Científico e Tecnológico) by the financial support and to Jonas Aguiar Junior for his help with ABAQUS analyses.

Appendix A. Projector matrix

From Equation (85),

$$\underset{\sim}{\mathbf{P}} = \frac{\partial \bar{\mathbf{d}}_R}{\partial \bar{\mathbf{d}}_D} = \begin{bmatrix} \underset{\sim}{\mathbf{P}}_{11} & \underset{\sim}{\mathbf{P}}_{12} \\ \underset{\sim}{\mathbf{P}}_{21} & \underset{\sim}{\mathbf{P}}_{22} \end{bmatrix} \qquad \underset{\sim}{\mathbf{P}}_{ij} = \frac{\partial \bar{\mathbf{d}}_{Ri}}{\partial \bar{\mathbf{d}}_{Dj}} = \begin{bmatrix} \frac{\partial \bar{\mathbf{u}}_{Ri}}{\partial \bar{\mathbf{u}}_{Dj}} & \frac{\partial \bar{\mathbf{u}}_{Ri}}{\partial \bar{\theta}_{Dj}} \\ \frac{\partial \bar{\theta}_{Ri}}{\partial \bar{\mathbf{u}}_{Dj}} & \frac{\partial \bar{\theta}_{Ri}}{\partial \bar{\theta}_{Dj}} \end{bmatrix}. \tag{A.1}$$

In order to identify the projector matrix $\underset{\sim}{\mathbf{P}}$, the variation of the corotational displacement in Equation (47) is written as

$$\delta \bar{\mathbf{u}}_{Ri} = \delta \mathbf{T}^T \mathbf{x}_{i1} + \mathbf{T}^T \delta \mathbf{u}_{i1} \tag{A.2}$$

where $\mathbf{x}_{i1} = \mathbf{X}_{i1} + \mathbf{u}_i - \mathbf{u}_1$ and $\mathbf{u}_{i1} = \mathbf{u}_i - \mathbf{u}_1$ reminding that $\mathbf{X}_i^{\varphi}$ and $\mathbf{X}_{i1}$ are constant. Let θ_T denote the relative rotation between the systems xyz and $\bar{x}\bar{y}\bar{z}$ so that $\mathbf{T} = \mathbf{R}_{\theta_T}\mathbf{I} = \mathbf{R}_{\theta_T}$. Using Equation (69) along with the coordinate transformation properties, one gets

$$\delta \bar{\mathbf{u}}_{Ri} = \mathbf{T}^T \underset{\sim}{\mathbf{S}}^T_{\delta \bar{\theta}_T} \mathbf{x}_{i1} + \mathbf{T}^T \delta \mathbf{u}_{i1} = -\underset{\sim}{\mathbf{S}}_{\delta \bar{\theta}_T} \bar{\mathbf{x}}_{i1} + \delta \bar{\mathbf{u}}_{Di1} = \mathbf{S}_{\bar{x}_{i1}} \underset{\sim}{\delta \bar{\theta}}_T + \delta \bar{\mathbf{u}}_{Di1}. \tag{A.3}$$

From Equation (52), the variation of the rotation tensor is

$$\delta \mathbf{R}_{\bar{\theta}_{Ri}} = \left(\delta \mathbf{T}^T \mathbf{R}_{\theta_i} + \mathbf{T}^T \delta \mathbf{R}_{\theta_i}\right)\mathbf{T}_0. \tag{A.4}$$

Following a procedure entirely similar to the one used in the variation of the corotational displacement gives

$$\delta\mathbf{R}_{\bar{\theta}Ri} = \left(\mathbf{T}^T \underset{\sim}{\mathbf{S}}^T_{\delta\bar{\theta}\,T} + \mathbf{T}^T \underset{\sim}{\mathbf{S}}_{\delta\bar{\theta}\,i}\right)\mathbf{R}_{\bar{\theta}i}\,\mathbf{T}_0 = \left(\underset{\sim}{\mathbf{S}}_{\delta\bar{\theta}\,i} - \underset{\sim}{\mathbf{S}}_{\delta\bar{\theta}\,R}\right)\mathbf{R}_{\bar{\theta}Ri} = \underset{\sim}{\mathbf{S}}_{\delta\bar{\theta}\,Di-\delta\bar{\theta}\,R}\,\mathbf{R}_{\bar{\theta}Ri}. \tag{A.5}$$

Using Equation (69), this expression becomes

$$\underset{\sim}{\delta\bar{\theta}}_{Ri} = \underset{\sim}{\delta\bar{\theta}}_{i} - \underset{\sim}{\delta\bar{\theta}}_{T}. \tag{A.6}$$

Expressions (A.3) and (A.6), in addition to some algebric manipulation [35,43], lead to

$$\underset{\sim}{\mathbf{P}}_{ij} = \delta_{ij}\mathbf{I}_6 - \mathbf{\Psi}_i\mathbf{\Gamma}_j - \delta_{1j}\,\phi \tag{A.7}$$

where

$$\mathbf{I}_6 = \begin{bmatrix}\mathbf{I} & \mathbf{0}\\ \mathbf{0} & \mathbf{I}\end{bmatrix} \qquad \mathbf{\Psi}_i = \begin{bmatrix}-\mathbf{S}_{\bar{x}_i}\\ \mathbf{I}\end{bmatrix} = \begin{bmatrix}\mathbf{S}_{\bar{x}_i} & \mathbf{I}\end{bmatrix}^T \qquad \mathbf{\Gamma}_j = \begin{bmatrix}\underset{\sim}{\frac{\partial\bar{\theta}}{\partial\bar{\mathbf{u}}_{Dj}}}_{T} \underset{\sim}{\frac{\partial\bar{\theta}}{\partial\bar{\theta}}}_{Dj}^{T}\end{bmatrix} = \underset{\sim}{\frac{\partial\bar{\theta}}{\partial\bar{\mathbf{d}}}}_{Dj}^{T} \qquad \phi = \begin{bmatrix}\mathbf{I} & \mathbf{0}\\ \mathbf{0} & \mathbf{0}\end{bmatrix}. \tag{A.8}$$

Therefore, the projector matrix $\underset{\sim}{\mathbf{P}}$ of the 3D beam element is

$$\underset{\sim}{\mathbf{P}} = \mathbf{I}_{12} - \mathbf{\Psi}\mathbf{\Gamma} - \mathbf{\Phi} \tag{A.9}$$

where

$$\mathbf{I}_{12} = \begin{bmatrix}\mathbf{I}_6 & \mathbf{0}\\ \mathbf{0} & \mathbf{I}_6\end{bmatrix} \qquad \mathbf{\Psi} = \begin{bmatrix}\mathbf{S}_{\bar{x}_1} & \mathbf{I} & \mathbf{S}_{\bar{x}_2} & \mathbf{I}\end{bmatrix}^T \qquad \mathbf{\Gamma} = \begin{bmatrix}\underset{\sim}{\frac{\partial\bar{\theta}_T}{\partial\bar{\mathbf{d}}_{D1}}} \underset{\sim}{\frac{\partial\bar{\theta}_T}{\partial\bar{\mathbf{d}}_{D2}}}\end{bmatrix} = \underset{\sim}{\frac{\partial\bar{\theta}_T}{\partial\bar{\mathbf{d}}_{D}}} \qquad \mathbf{\Phi} = \begin{bmatrix}\phi & \mathbf{0}\\ \phi & \mathbf{0}\end{bmatrix} \tag{A.10}$$

with

$$S_{\bar{x}_1} = \begin{bmatrix}0 & 0 & 0\\ 0 & 0 & 0\\ 0 & 0 & 0\end{bmatrix} \qquad S_{\bar{x}_2} = \begin{bmatrix}0 & 0 & 0\\ 0 & 0 & -L\\ 0 & L & 0\end{bmatrix}. \tag{A.11}$$

Details on the derivation of

$$\mathbf{\Gamma} = \underset{\sim}{\frac{\delta\bar{\theta}}{\delta\bar{\mathbf{d}}_D}}^{T} = \frac{1}{L}[\Xi_1 \;\; \Xi_2 \;\; \Xi_3 \;\; 0], \tag{A.12}$$

where

$$\Xi_1 = \begin{bmatrix}0 & 0 & \eta\\ 0 & 0 & 1\\ 0 & -1 & 0\end{bmatrix} \qquad \Xi_2 = \begin{bmatrix}L & -\eta L & 0\\ 0 & 0 & 0\\ 0 & 0 & 0\end{bmatrix} \qquad \Xi_3 = \begin{bmatrix}0 & 0 & -\eta\\ 0 & 0 & -1\\ 0 & 1 & 0\end{bmatrix} \qquad \eta = \frac{q_1}{q_2}, \tag{A.13}$$

can be found in Refs. [20,29,35].

One can demonstrate that $\mathbf{P}^2 = \mathbf{P}$ and that the matrix has six zero eigenvalues, whose corresponding eigenvectors are the rigid body modes of the finite element. In the transformation (85), the projector matrix purges the rigid body modes of the finite element. The three translation modes are associated with the non-zero columns of $\mathbf{\Phi}$ and the three rotation modes are associated with the columns of $\mathbf{\Psi}$.

Appendix B. Expressions of $\underset{\sim}{\delta\mathbf{f}}_{Di}$

Substitution of

$$\underset{\sim}{\delta\bar{\mathbf{f}}}_{R} = \underset{\sim}{\frac{\partial\bar{\mathbf{f}}}{\partial\bar{\mathbf{d}}}}_{R}\underset{\sim}{\delta\bar{\mathbf{d}}}_{R} = \underset{\sim}{\frac{\partial\bar{\mathbf{f}}}{\partial\bar{\mathbf{d}}}}_{R}\underset{\sim}{\frac{\partial\bar{\mathbf{d}}}{\partial\bar{\mathbf{d}}}}_{D}\underset{\sim}{\frac{\partial\bar{\mathbf{d}}}{\partial\mathbf{d}}}_{D}\underset{\sim}{\delta\mathbf{d}}_{D} = \underset{\sim}{\bar{\mathbf{k}}}_{R}\,\underset{\sim}{{}^{*}\mathbf{P}}\,\mathbf{G}^T\,\underset{\sim}{\delta\mathbf{d}}_{D} \tag{B.1}$$

into Equation (96) gives

$$\underset{\sim}{\delta\mathbf{f}}_{D1} = \mathbf{G}\,\underset{\sim}{{}^{*}\mathbf{P}^T}\,\underset{\sim}{\bar{\mathbf{k}}}_{R}\,\underset{\sim}{{}^{*}\mathbf{P}}\,\mathbf{G}^T\,\underset{\sim}{\delta\mathbf{d}}_{D}. \tag{B.2}$$

To evaluate $\underset{\sim}{\delta\mathbf{f}}_{D2}$ one must first identify $\underset{\sim}{\delta^{*}\mathbf{P}}$. From the property $\mathbf{\Gamma\Psi} = \mathbf{I}$, postmultiplication and premultiplication of Equation (91) by $\mathbf{\Psi}$ and $\mathbf{\Gamma}$ yield, respectively,

$$\underset{\sim}{{}^{*}\mathbf{P}}\mathbf{\Psi} = \mathbf{\Psi} - \mathbf{\Psi}\,\mathbf{\Gamma}\,\mathbf{\Psi} = 0 \qquad \mathbf{\Gamma}\,\underset{\sim}{{}^{*}\mathbf{P}} = \mathbf{\Gamma} - \mathbf{\Gamma}\,\mathbf{\Psi}\,\mathbf{\Gamma} = \mathbf{0} \tag{B.3}$$

whose variations are

$$\delta(\underset{\sim}{{}^{*}\mathbf{P}}\,\mathbf{\Psi}) = \underset{\sim}{\delta^{*}\mathbf{P}}\,\mathbf{\Psi} + \underset{\sim}{{}^{*}\mathbf{P}}\,\delta\mathbf{\Psi} \qquad \delta(\mathbf{\Gamma}\,\underset{\sim}{{}^{*}\mathbf{P}}) = \delta\mathbf{\Gamma}\,\underset{\sim}{{}^{*}\mathbf{P}} + \mathbf{\Gamma}\,\underset{\sim}{\delta^{*}\mathbf{P}}. \tag{B.4}$$

Postmultiplying the first equation by $\mathbf{\Gamma}$ and premultiplying the second by $\mathbf{\Psi}$ produce, in view of Equation (91),

$$\underset{\sim}{\delta^{*}\mathbf{P}}\left(\mathbf{I}_{12} - \underset{\sim}{{}^{*}\mathbf{P}}\right) + \underset{\sim}{{}^{*}\mathbf{P}}\,\delta\mathbf{\Psi}\,\mathbf{\Gamma} = 0 \qquad \mathbf{\Psi}\,\delta\mathbf{\Gamma}\,\underset{\sim}{{}^{*}\mathbf{P}} + \left(\mathbf{I}_{12} - \underset{\sim}{{}^{*}\mathbf{P}}\right)\underset{\sim}{\delta^{*}\mathbf{P}} = 0. \tag{B.5}$$

The property $\underset{\sim}{{}^{*}\mathbf{P}}2 = \underset{\sim}{{}^{*}\mathbf{P}}$ allows one to write

$$\underset{\sim}{\delta^{*}\mathbf{P}} = \delta(\underset{\sim}{{}^{*}\mathbf{P}}\,\underset{\sim}{{}^{*}\mathbf{P}}) = \underset{\sim}{\delta^{*}\mathbf{P}}\,\underset{\sim}{{}^{*}\mathbf{P}} + \underset{\sim}{{}^{*}\mathbf{P}}\,\underset{\sim}{\delta^{*}\mathbf{P}} \tag{B.6}$$

and, after adding Equation (B.5), gives

$$\delta^{*}\underset{\sim}{\mathbf{P}} = -\,{}^{*}\underset{\sim}{\mathbf{P}}\,\delta\boldsymbol{\Psi}\,\boldsymbol{\Gamma} - \boldsymbol{\Psi}\,\delta\boldsymbol{\Gamma}\,{}^{*}\underset{\sim}{\mathbf{P}}. \tag{B.7}$$

The general expression for $\delta^{*}\mathbf{P}$ proposed by Nour-Omid and Rankin [30] clearly fails for beam elements because involves in this case inversion of singular matrix. Also, for many elements the simplification of neglecting the second term in Equation (B.7) is commonly adopted. Substitution of Equation (B.7) into Equation (96) yields

$$\delta\underset{\sim}{\mathbf{f}}_{D2} = -\mathbf{G}\,(\boldsymbol{\Gamma}^{T}\,\delta\boldsymbol{\Psi}^{T}\,{}^{*}\underset{\sim}{\mathbf{P}}T^{*}\underset{\sim}{\mathbf{P}}T + {}^{*}\underset{\sim}{\mathbf{P}}T\,\delta\boldsymbol{\Gamma}^{T}\,\boldsymbol{\Psi}^{T})\,\underset{\sim}{\bar{\mathbf{f}}}_{R} = -\mathbf{G}\,(\boldsymbol{\Gamma}^{T}\,\mathbf{H}_{1}^{T}\,{}^{*}\underset{\sim}{\mathbf{P}} + \Upsilon)\,\mathbf{G}^{T}\,\delta\underset{\sim}{\mathbf{d}}_{D} \tag{B.8}$$

where

$$\mathbf{H}_{1} = \begin{bmatrix} \mathbf{0} \\ \mathbf{0} \\ \mathbf{S}_{\underset{\sim}{\tilde{n}}\,D2} \\ \mathbf{0} \end{bmatrix} \qquad \Upsilon = \frac{\underset{\sim}{\bar{m}}_{R11} + \underset{\sim}{\bar{m}}_{R21}}{L}\begin{bmatrix} \Upsilon_{1} & \mathbf{0} \\ \Upsilon_{2} & \mathbf{0} \end{bmatrix} \tag{B.9}$$

with

$$\Upsilon_{1} = \begin{bmatrix} 0&0&0&0&0&0 \\ 0&0&0&0&0&0 \\ 0&0&0&0&0&-1-\eta^{2} \\ 0&0&0&0&0&0 \\ 0&0&0&0&0&L(1+\eta^{2}) \\ 0&0&0&0&0&0 \end{bmatrix} \qquad \Upsilon_{2} = \begin{bmatrix} 0&0&0&0&0&0 \\ 0&0&0&0&0&0 \\ 0&0&0&0&0&1+\eta^{2} \\ 0&0&0&0&0&0 \\ 0&0&0&0&0&0 \\ 0&0&0&0&0&0 \end{bmatrix}. \tag{B.10}$$

The terms $\bar{m}_{R11}$ and $\bar{m}_{R21}$ are the first elements in $\underset{\sim}{\bar{\mathbf{m}}}_{R1}$ and $\underset{\sim}{\bar{\mathbf{m}}}_{R2}$, respectively, and details on the evaluation of $\mathbf{H}_1$ and Υ can be found in Ref. [35,43]. Although some references like [30,32] take $\tilde{\Upsilon}$ as null due to rotational equilibrium of the elements, this term may not be negligible for coarse meshes.

Tensor transformation of (69) to the corotational system gives

$$\underset{\sim}{\mathbf{S}}_{\delta\bar{\theta}\,T} = \mathbf{T}^{T}\,\delta\mathbf{T}. \tag{B.11}$$

Thus, one can write

$$\delta\underset{\sim}{\mathbf{f}}_{D3} = \delta\mathbf{G}\,{}^{*}\underset{\sim}{\mathbf{P}}^{T}\,\underset{\sim}{\bar{\mathbf{f}}}_{R} = \delta\mathbf{G}\,\underset{\sim}{\bar{\mathbf{f}}}_{D} = \mathbf{G}\begin{bmatrix} \underset{\sim}{\mathbf{S}}_{\delta\bar{\theta}\,T} & \mathbf{0} & \mathbf{0} & \mathbf{0} \\ \mathbf{0} & \underset{\sim}{\mathbf{S}}_{\delta\bar{\theta}\,T} & \mathbf{0} & \mathbf{0} \\ \mathbf{0} & \mathbf{0} & \underset{\sim}{\mathbf{S}}_{\delta\bar{\theta}\,T} & \mathbf{0} \\ \mathbf{0} & \mathbf{0} & \mathbf{0} & \underset{\sim}{\mathbf{S}}_{\delta\bar{\theta}\,T} \end{bmatrix}\underset{\sim}{\bar{\mathbf{f}}}_{D} = -\mathbf{G}\,\mathbf{H}_{2}\,\delta\underset{\sim}{\bar{\theta}}_{T} \qquad \mathbf{H}_{2} = \begin{bmatrix} \underset{\sim}{\mathbf{S}}_{\tilde{\mathbf{n}}\,D1} \\ \underset{\sim}{\mathbf{S}}_{\tilde{\mathbf{m}}\,D1} \\ \underset{\sim}{\mathbf{S}}_{\tilde{\mathbf{n}}\,D2} \\ \underset{\sim}{\mathbf{S}}_{\tilde{\mathbf{m}}\,D2} \end{bmatrix}. \tag{B.12}$$

From Equation (A.10)

$$\delta\underset{\sim}{\bar{\theta}}_{T} = \frac{\partial\underset{\sim}{\bar{\theta}}_{T}}{\partial\underset{\sim}{\bar{\mathbf{d}}}_{D}}\,\delta\underset{\sim}{\bar{\mathbf{d}}}_{D} = \boldsymbol{\Gamma}\,\mathbf{G}^{T}\,\delta\underset{\sim}{\mathbf{d}}_{D}. \tag{B.13}$$

Substitution of this expression into Equation (B.12) yields

$$\delta\underset{\sim}{\mathbf{f}}_{D3} = -\mathbf{G}\,\mathbf{H}_{2}\,\boldsymbol{\Gamma}\,\mathbf{G}^{T}\,\delta\underset{\sim}{\mathbf{d}}_{D}. \tag{B.14}$$

References

[1] R.F. Silva, F.A.F. Teófilo, E. Parente Jr., A.M.C. Melo, A.S. Holanda, Optimization of composite catenary risers, Mar. Struct. 33 (2013) 1–20.
[2] K. Bhaskar, L. Librescu, A geometrically non-linear theory for laminated anisotropic thin-walled beams, Int. J. Eng. Sci. 33 (9) (1995) 1331–1344.
[3] T.P. Vo, J. Lee, Geometrically nonlinear analysis of thin walled composite box beams, Comput. Struct. 87 (3–4) (2009) 236–245.
[4] T.P. Vo, J. Lee, Geometrically nonlinear analysis of thin walled composite box beams using shear-deformable beam theory, Int. J. Mech. Sci. 52 (1) (2010) 65–74.
[5] C.M. Saravia, S.P. Machado, V.H. Cortinez, A geometrically exact nonlinear finite element for composite closed section thin-walled beams, Comput. Struct. 89 (23–24) (2011) 2337–2351.
[6] M.A. Crisfield, G. Jelenic, Objectivity of strain measures in the geometrically exact three-dimensional beam theory and its finite-element implementation, Proc. Roy. Soc. Lond. 455 (1998) 1125–1147.
[7] C.M. Saravia, S.P. Machado, V.H. Cortinez, A consistent total Lagrangian finite element for composite closed section thin walled beams, Thin-Walled Struct. 52 (2012) 102–116.
[8] J.C. Massa, E.J. Barbero, A strength of materials formulation for thin walled composite beams with torsion, J. Compos. Mater. 32 (17) (1998) 1560–1594.
[9] L.P. Kollar, A. Pluzsik, Analysis of thin walled composite beams with arbitrary layup, J. Reinforc. Plast. Compos. 21 (16) (2002) 1423–1465.
[10] V.V. Volovoi, D.H. Hodges, C.E.S. Cesnik, B. Popescu, Assessment of beam modeling methods for rotor blade applications, Math. Comput. Model. 33 (10–11) (2001) 1099–1112.
[11] J. Lee, S. Lee, Flexural-torsional behavior of thin-walled composite beams, Thin-Walled Struct. 42 (9) (2004) 1293–1305.
[12] H.A. Salim, J.F. Davalos, Torsion of open and closed thin-walled laminated composite section, J. Compos. Mater. 39 (6) (2005) 497–524.
[13] T.P. Vo, J. Lee, Flexural-torsional behavior of thin-walled closed-section composite box beams, Eng. Struct. 29 (8) (2007) 1774–1782.
[14] T.P. Vo, J. Lee, Flexural-torsional behavior of thin-walled closed-section composite box beams using shear-deformable beam theory, Eng. Struct. 30 (7) (2008) 1958–1968.
[15] T.P. Vo, J. Lee, Flexural-torsional behavior of thin-walled composite space frames, Int. J. Mech. Sci. 51 (11–12) (2009) 837–845.
[16] A.H. Sheikh, O.T. Thomsen, An efficient beam element for the analysis of laminated composite beams of thin-walled open and closed cross sections, Compos. Sci. Technol. 68 (10–11) (2008) 2273–2281.
[17] T.P. Vo, J. Lee, Geometrical nonlinear analysis of thin-walled composite beams using finite element method based on first order shear deformation theory, Arch. Appl. Mech. 81 (2011) 419–435.
[18] C.E.S. Cesnik, D.H. Hodges, Vabs: a new concept for composite rotor blade cross-sectional modeling, J. Am. Helicopter Soc. 42 (1) (1997) 27–38.
[19] A. Pluzsik, L.P. Kollar, Effects of shear deformation and restrained warping on the displacement of composite beams, J. Reinforc. Plast. Compos. 21 (17) (2002)

1517–1541.
[20] L.A.T. Mororó, A.M.C. Melo, E. Parente Jr., Geometrically nonlinear analysis of thin-walled laminated composite beams, Lat. Am. J. Solid. Struct. 12 (11) (2015) 2094–2117.
[21] M.A. Crisfield, Non-linear Finite Element Analysis of Solids and Structures, first ed., John Wiley & Sons, 1991.
[22] J. Argyris, An excursion into large rotation, Comput. Methods Appl. Mech. Eng. 32 (1–3) (1982) 85–155.
[23] R.M. Jones, Mechanics of Composite Materials, second ed., Taylor & Francis, Philadelphia, 1999.
[24] J.N. Reddy, Mechanics of Laminated Composite Plates and Shells, second ed., CRC Press, 2004.
[25] J.M. Battini, Co-rotational Beam Elements in Instability Problems, Mechanical Engineering, Royal Institute of Technology, Stockholm, Sweden, 2002.
[26] J.M. Battini, C. Pacoste, Co-rotational beam elements with warpings effects in instability problems, Comput. Methods Appl. Mech. Eng. 191 (2002) 1755–1789.
[27] W. McGuire, R.H. Gallagher, R.D. Ziemian, Matrix Structural Analysis, second ed., John Wiley & Sons, Inc., 2000.
[28] C.C. Rankin, F.A. Brogan, An element independent corotational procedure for the treatment of large rotations, J. Pressure Vessel Technol. 108 (1986) 165–174.
[29] C.C. Rankin, B. Nour-Omid, The use of projectors to improve finite element performance, Comput. Struct. 30 (1988) 257–267.
[30] B. Nour-Omid, C.C. Rankin, Finite rotation analysis and consistent linearization using projectors, Comput. Methods Appl. Mech. Eng. 93 (1991) 353–384.
[31] M.A. Crisfield, A consistent co-rotational formulation for non-linear, three-dimensional, beam-elements, Comput. Methods Appl. Mech. Eng. 81 (1990) 131–150.
[32] M.A. Crisfield, G.F. Moita, A unified co-rotational framework for solids, shells and beams, Int. J. Solid Struct. 33 (1996) 2969–2992.
[33] M.A. Crisfield, Non-linear Finite Element Analysis of Solids and Structures, fourth ed., John Wiley & Sons, 1997.
[34] C. Pacoste, A. Eriksson, Beam elements in instability problems, Comput. Methods Appl. Mech. Eng. 144 (1997) 163–197.
[35] F.A.C. Monteiro, Uma Formulação Co-rotacional Geral: Aplicação a Pórticos Espaciais, Master thesis Instituto Tecnológico de Aeronáutica, 2004.
[36] C.A. Felippa, B. Haugen, A unified formulation of small-strain corotational finite elements: I. theory, Comput. Methods Appl. Mech. Eng. 194 (2005) 2285–2335.
[37] M.L.T. Moreira, Parametrização das rotações em teorias de barras e cascas, Doctorate thesis Escola Politécnica da Universidade de São Paulo, 2009.
[38] K.W. Spring, Euler parameters and the use of quaternion algebra in the manipulation of finite rotation: a review, Mech. Mach. Theor. 21 (5) (1986) 365–373.
[39] R.A. Spurrier, Comment on singularity-free extraction of quaternion from a direct-cosine mattrix, J. Spacecraft 15 (1978) 255.
[40] Simulia, Abaqus/standard User's Manual - version 6.12.
[41] I.M. Daniel, O. Ishai, Engineering Mechanics of Composite Materials, second ed., Oxford University, 2006.
[42] K. Mattiasson, Numerical results from large deflection beam and frame problems analysed by means of elliptic integrals, Int. J. Numer. Methods Eng. 17 (1981) 145–153.
[43] L.A.T. Mororó, Análise não linear geométrica de vigas laminadas de parede fina, Master thesis Universidade Federal do Ceará, 2013.
[44] A. Pagani, E. Carrera, Large-deflection and post-buckling analyses of laminated composite beams by Carrera Unified Formulation, Compos. Struct. 170 (2017) 40–52.
[45] K.J. Bathe, S. Bolourchi, Large displacement analysis of three-dimensional beam structures, Int. J. Numer. Methods Eng. 14 (1979) 961–986.
[46] J.C. Simo, L. Vu-Quoc, A three-dimensional finite strain rod model. part 2: computational aspects, Comput. Methods Appl. Mech. Eng. 58 (1986) 79–116.
[47] D. Lanc, G. Turkalj, I. Pesic, Global buckling analysis model for thin-walled composite laminated beam type structures, Compos. Struct. 111 (2014) 371–380.